



**Politecnico
di Torino**

POLITECNICO DI TORINO

Master Degree Thesis in Electronic Engineering

**Femtosecond laser Fiber Bragg Grating
fabrication and in-line interferometric
optical fiber structures for advanced
sensing**

Supervisors

Prof. Guido PERRONE

Dott. Massimo OLIVERO

Candidate

Matteo CAVAGNETTO

ACADEMIC YEAR 2022-2023

Acknowledgements

Abstract

Fiber Optic Sensors (FOSs) successfully suite critical sensing applications like in biomedicine or harsh environments. They combine robustness to noise and interference with minimal invasive impact, real-time measurement capabilities, and remote interrogation. FOSs are all-dielectric devices that are immune to electromagnetic interference and their small size allows embedding into various structures including biological tissues, overcoming the major limitations of conventional electronic sensors.

Fiber Bragg Gratings (FBG)s are the most widespread FOS because of their high rejection to intensity noise and the ability to achieve quasi-distributed sensing through multiplexing. However, their fabrication requires a complex and expensive setup to induce a periodic refractive index perturbation in the fiber core that produces light reflection at a given wavelength dependent on temperature and applied strain. Another FOS analyzed is the interferometric sensor, which consists of splicing a multi-mode fiber section between two single-mode sections. The sensor is characterized by low fabrication costs and higher sensitivity, which can be up to 10 times that of FBGs.

The thesis explores the optimization of fabrication process of these two types of FOSs and presents a combination of them for better performance.

The FBGs in this work are written using a femtosecond laser, which is a smart and programmable solution, alternative to the more common phase-mask technique, to fabricate custom sensors, specific for a particular application. The optimization of the gratings required many runs of the fabrication-characterization processes, using different kinds of fibers (standard single-mode, bend-insensitive, double cladding, etc.) and led to high repeatable FBGs with different characteristics, but all with optimized spectral response to be used both in 2 mm long single-point configuration and multipoint sensor array. As an example of application, some FBG sensor array have been used to monitor the temperature increase during simulated laser ablation of tumors.

As for the SMS sensors, a novel inline interferometric fiber structure made by offset-splicing a 10 cm long G.657A2 Bend-Insensitive Fiber (BIF) acting as the multi-mode section between two single mode pigtails at 1550 nm is also investigated. At the considered wavelength the BIF can behave like a two-mode fiber given its short length. The first junction excites both the fundamental and the first higher order mode and the two combine again at the second junction originating the interference spectrum, whose shift can be used to detected temperature and strain variations. Different samples are fabricated and characterized as temperature sensors showing a large sensitivity up to 100 pm/Å°C.

The structure is tested realizing the optical version of the hot wire flow-meter, in which the flow of air is measured through the change in temperature induced by the flowing air in the BIF section. The optical heating is obtained by exploiting the absorption of a laser by a graphite layer deposited on the BIF section. A blue shift in the interference spectrum is well measured as air flows in the tube and dissipates heat. The behavior of the optical flow-meter is compared by connecting a commercial flow-meter in series in the same pipe, showing repeatability and sensitivity of 0.33 nm/slm.

In conclusion by leveraging the distinct sensitivities of SMS and FBG it is possible to effectively mitigate cross-sensitivity issues and achieve accurate measurements.

Contents

List of Figures	V
List of Tables	VIII
1 Introduction	1
2 FBG theoretical background	3
2.1 Induced refractive index change	4
2.2 Sensing principle	4
2.2.1 Fabrication technique	5
3 Femtosecond laser FBG fabrication	7
3.1 SM2000 fiber	8
3.1.1 SM2000 fiber: FBG written in the cladding region	13
3.1.2 SM2000 fiber: sensing unit combining FBG and SMS	16
3.2 Bend insensitive fiber (BIF)	17
3.3 Polyamide coated fiber for high temperature FBGs	23
3.4 SFM28 fiber	27
3.4.1 Most common errors in writing gratings	27
3.4.2 SFM-28 FBG optimized realization process	31
3.5 SFM-28 FBG practical implementation as single point temperature sensor	33
3.6 SFM-28 FBG practical implementation as multi points array temperature sensor	34
3.6.1 Calibration procedure of the temperature sensor	38
4 SMS theoretical background	43
5 SMS fabrication	47
5.0.1 SMS using SM2000 fiber for the multimode section	49
5.0.2 SMS using BIF G657 fiber for the multimode section	51
5.0.3 BIF G657 SMS temperature sensor	52
6 Optical flow-meter	55
6.1 FBG fast response flow-meter	55
6.2 SMS parallel fibers flow meter	58

7 Conclusion	61
7.1 Achieved results	61
7.2 Outlook	61
Bibliography	65

List of Figures

2.1	Schematic diagram of working principle of fiber Bragg grating [1].	3
3.1	Femtosecond laser writing setup.	7
3.2	LP01 3D modal field distribution.	9
3.3	LP01 modal field distribution respect to fiber core	9
3.4	LP11 3D modal field distribution.	10
3.5	LP11 modal field distribution respect to fiber core.	10
3.6	Femtosecond laser camera showing the written FBG in two different core position middle and edge core-cladding.	11
3.7	Output spectrum showing different peaks whose amplitude depend on the overlap integral between grating and modal field distributions.	11
3.8	Femtosecond laser camera showing FBG LPO1 written in the middle of the fiber core.	12
3.9	Output spectrum of the FBG connected to the pigtail without offset showing only the LP01 mode peak	12
3.10	Output spectrum of the previous FBG now connected to the pigtail with offset splice showing two peaks LP11 and LP01.	13
3.11	Laser camera showing a LP11 mode FBG written in the edge core cladding.	13
3.12	Spectrum of a LP11 FBG with no offset connected few centimeters far from an offset splice.	14
3.13	Femtosecond laser camera showing the writing scheme of LP11 fbg using offset.	14
3.14	Spectrum of a FBG written 4 μm offset from edge core cladding.	15
3.15	Spectrum of a FBG written 6 μm offset from edge core cladding.	15
3.16	Spectrum of the sensing unit combining FBG and SMS.	16
3.17	BIF G657A2 analysed using microscope.	17
3.18	BIF cladding diameter measured using microscope.	18
3.19	BIF core diameter measured using microscope.	19
3.20	BIF trench diameter measured using microscope.	19
3.21	Femtosecond-laser camera focused on fiber core no optimized case.	20
3.22	Femtosecond-laser camera focused on fiber core optimized case.	21
3.23	Femtosecond-laser camera showing a written grating.	21
3.24	FBG 1550 nm spectrum.	22
3.25	Commercial polyamide FBG.	24

3.26	Spectrum of polyamide FBG 1 written using Femtosecond laser.	24
3.27	Spectrum of polyamide FBG 2 highlighting the fabrication repeatability. .	25
3.28	Interpolation of points representing the computed n_{eff} values for different wavelengths.	26
3.29	Laser camera showing a correct focused laser spot without any astigmatic distortions.	28
3.30	Laser camera showing a FBG written using too high emitted power. . . .	28
3.31	Spectrum of a FBG written using too high emitted power.	29
3.32	Schematic of a correct grating extremes selection respect to the stage trajectory.	29
3.33	Laser camera showing a written FBG whose end_position is located in the deceleration phase.	30
3.34	Measured reflected FBG spectrum with too much noise due to errors in moving the stage.	30
3.35	Laser camera showing a written FBG whose end_position is correctly located in the constant velocity phase.	31
3.36	Laser camera showing the induced periodic refractive index modulation. .	32
3.37	Measured reflected spectrum of a FBG written using the optimized fabrication process.	32
3.38	Setup used to optically heat and test chemical compounds.	33
3.39	Measured wavelength shift due to laser heating for different graphite based compounds respect to water.	34
3.40	Schematic of the 13 point FBG sensing array used as distribute temperature sensor.	34
3.41	Measured reflected spectrum of the 13 point FBG sensing array.	35
3.42	First order polynomial interpolation highlighting the variation of n_{eff} for different wavelength values.	36
3.43	First order polynomial interpolation of n_{eff} values for different wavelengths considering all the nine fabricated array.	37
3.44	Sensing FBG arrays measuring temperature profiles.	37
3.45	Multipoint temperature sensor.	38
3.46	Calibration steps: wavelength vs reference temperature.	39
3.47	Calibration curve of the temperature sensor.	39
3.48	Optical sensor versus reference sensor in measuring temperature.	40
3.49	Optical temperature sensor accuracy.	41
4.1	Schematic of the SMS structure.	43
4.2	Matlab simulation showing modal profiles during the computation of the overlap integral.	44
4.3	Measured spectrum of SMS realized using different multimode section length.	45
5.1	Matlab simulation to compute the overlap integral between two modes in a common splice	47
5.2	Matlab simulation to compute the overlap integral between two modes in a offset splice.	48

5.3	Fujikura 90s splicer camera displaying an offset junction.	48
5.4	SMS interference pattern respect to V number.	49
5.5	Interference spectrum of a SM2000 SMS.	50
5.6	SM2000 SMS interference pattern respect to V number.	51
5.7	Interference pattern of SM2000 SMS respect to BIF G657 case.	52
5.8	Measured spectra of the SMS interference pattern for different temperature values.	53
5.9	Details on the measured spectra of the SMS interference pattern for different temperature values.	53
5.10	SMS peak wavelength measured for different temperature steps.	54
5.11	Calibration curve of the SMS used as temperature sensor.	54
6.1	Schematic of the FBG hot-wire flow-meter.	56
6.2	Hot wired FBG sensing unit.	56
6.3	Schematic of the FBG hot-wire flow-meter.	57
6.4	Optical flow-meter versus reference sensor.	58
6.5	SMS optical flowmeter versus reference sensor.	59

List of Tables

3.1	Polyamide fiber n_{eff} values versus wavelength	26
3.2	Measured peaks of 13 points FBG sensing array.	36
3.3	Measured temperature sensitivity coefficients.	40

Chapter 1

Introduction

Critical sensing applications, such as in the biomedical field or in harsh environments [2], require new solutions capable of combining robustness to noise and interferences, minimal invasive impact, continuous and real-time measurement, and possibility of remote interrogation. For this reason monitoring technologies able to understand and predict environmental changes remains a demanding challenge and several technologies have been developed to achieve the goal.

Many electrochemical sensor have been developed and applied thanks to the high selectivity and low-power operation, however since their electrodes suffer oxidation are not always strong enough solution. From the other hand electromechanical sensors and thermoelectric sensor which are extensively developed, have a short lifetime in harsh environments due to corrosion. Deformation and electrical disturbance make them not suitable for monitoring application which are required to be running for long period with high reliability levels.

Fiber Optic Sensors (FOSs) are known to match all the previous requirements, overcoming the major limitations of conventional electronic sensors. Since FOSs can be fabricated as all-dielectric devices, they are intrinsically immune from electromagnetic interference and not capable to start fires; moreover, their small size (down to $\simeq 0.25$ mm) opens to their embedding into a large variety of structures, from composite material to biological tissues. Finally, they can be integrated into a common telecommunication fiber infrastructure, enabling remote sensing with data transmission even over thousands of kilometers [3].

Among the many types of FOSs, particularly attractive are the so-called Fiber Bragg Gratings (FBGs), which are fabricated by inducing a periodic refractive index perturbation in the fiber core [4, 5]; this allows obtaining a notchlike spectral response in which the position of the dip depends on the local temperature and on the strain applied to the fiber. FBGs are by far the most widespread type of FOS because of their high rejection to intensity noise and the ability to achieve quasi-distribute sensing through multiplexing.

For all these reasons fiber gratings are excellent elements for sensing which is an important part of health monitoring system for civil, mechanical and aerospace applications [6]. They could enable the detection of foreseeable situations occurring and the prevention of harmful consequences.

Chapter 2

FBG theoretical background

The Fiber Bragg Grating, which was first demonstrated at the Canadian Communications Research Center in 1978 by Hill, are made by realizing a periodic modulation of the refractive index, called grating, in the core of a single mode fiber [6]. The light which is reflected back at each period combines coherently to one large reflection at a particular wavelength. In fact only the wavelengths, referred to as the Bragg wavelength [7,8], that satisfy the so called Bragg condition are affected and strongly back reflected through the same core of the fiber [6]. In details if a broadband source signal is launched as input from one side of the fiber, only the wavelength which satisfies the Bragg condition will be reflected while the other wavelengths are transmitted without any enhanced reflections as shown in Fig. 2.1 [1].

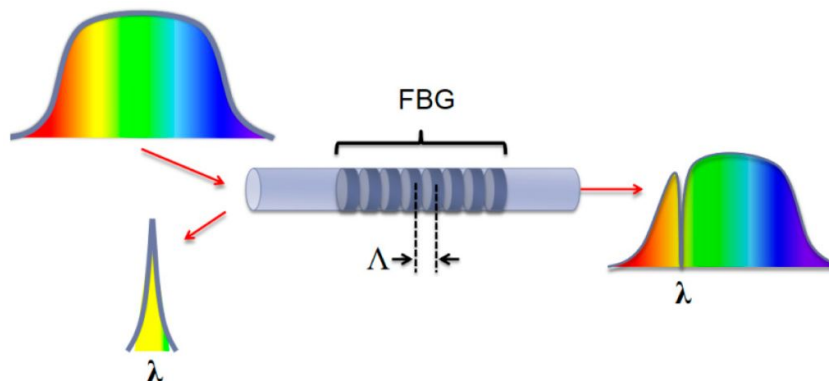


Figure 2.1: Schematic diagram of working principle of fiber Bragg grating [1].

$$\beta_1 - \beta_2 = \Delta\beta = \frac{2\pi}{\Lambda} \quad (2.1)$$

Where β_1 and β_2 are the propagation constants of the modes being coupled and Λ is the gratings period [6]. But due to the forward propagating core mode which is the LP01 is coupled to the backward propagating core mode, as explained [9,10], the constants β are the same in amplitude differing only by the sign:

$$\beta_2 = -\beta_1 = \beta \quad (2.2)$$

$$\beta = -(-\beta) = \frac{2\pi}{\Lambda} \quad (2.3)$$

$$2\beta = \frac{2\pi}{\Lambda} \quad (2.4)$$

but since β can be written as:

$$\beta = \frac{2\pi}{\Lambda} n_{eff} \quad (2.5)$$

Where n_{eff} is the effective refractive index of the LP01 mode. Making some simplifications is possible to obtain the relation of the Bragg wavelength:

$$\lambda_{Bragg} = 2 \cdot n_{eff} \cdot \Lambda \quad (2.6)$$

The λ_{Bragg} can be chosen accordingly to the desired specifics by changing the grating spacing during fabrication to allow the realization of costume narrow band reflectors.

2.1 Induced refractive index change

As previously reported to generate the grating is necessary to induce a periodic modulation of the core refractive index. The simplest uniform fiber Bragg grating structure [6] has a core index profile described by the following relation [11]:

$$n(x) = n_o + \Delta_n \cdot \cos\left(\frac{2\pi x}{\Lambda}\right) \quad (2.7)$$

where Δ_n is the amplitude of the induced refractive index perturbation whose typical value is between 10^{-2} and 10^{-5} , n_o is the core index and Λ the grating period. The spectral reflectivity of the FBG strictly depends on the grating strength so increasing the magnitude of the refractive index change is possible to get reflected peaks with higher amplitude. Moreover also the length of the gratings play a fundamental role in determining both the grating reflectivity and the FWHM bandwidth. Normally the grating length is limited to few centimeters but it is enough to generate narrow-band FBG whose reflectivity is close to 100%.

2.2 Sensing principle

FBGs are excellent elements in sensing application, in fact, since the Bragg wavelength is a function of the grating period (Λ) and the effective refractive index (n_{eff}), any change in the refractive index or in the grating period leads to a shift in the Bragg wavelength allowing physical quantities such as temperature (T) and strain (ϵ) to be measured. In details the Bragg wavelength is a function of both Temperature and strain according to the relation:

$$\frac{d\lambda_{Bragg}}{\lambda_{Bragg}} = \left[\frac{1}{\Lambda} \frac{\delta\Lambda}{\delta\epsilon} + \frac{1}{n_{eff}} \frac{\delta n_{eff}}{\delta\epsilon} \right] d\epsilon + \left[\frac{1}{\lambda} \frac{\delta\Lambda}{\delta T} + \frac{1}{n_{eff}} \frac{\delta n_{eff}}{\delta T} \right] dT \quad (2.8)$$

The strain induced a shift in the λ_{Bragg} due to two effects the photo elastic effect [12–14] and the physical elongation of the optical fiber which corresponds to a change in the grating spacing [6]. On the other hand the temperature response is again due to two factors the thermal expansion and the thermo-optic effects. The first one so the thermo-optic effect is responsible for about the 95% of the total shift while the thermal expansion accounts for only 5% of the total shift [6].

2.2.1 Fabrication technique

The production of high quality FBGs has found a growing interest in recent years among laboratories and research centres involved in the improvement and development of various techniques. Currently the most spread external writing technique allowing the realization of the grating directly exposing the fiber to a light source are the phase mask technique and the point by point technique which is explained in chapter. 3.

In the phase mask technique the key component is phase mask which is placed in contact with the fiber and then a laser beam illuminating the all the setup imprints the refractive index modulation in the fiber core. More detailed explanations of this process, which is not the aim of this thesis, can be found [6, 15–17]

Chapter 3

Femtosecond laser FBG fabrication

The use of femtosecond laser in Fiber Bragg Grating fabrication has been successfully developed by several laboratories in the recent years as its properties allows the realization of costume gratings in a truly efficient way. In the point by point technique a femtosecond laser is used to inscribe individual grating one step at time [18] along the core of the fiber using the laser as a working tool [6]. Doing this the single pulse of the emitted light is focused onto the core inducing in the absorption area a permanent change of the refractive index [19]. To correctly perform this solution a high precise computer controlled translation stage (Fig. 3.1) is required to move the fiber accordingly to the desired grating pitch Λ determining the associated λ_{Bragg} . In conclusion controlling the emitted power and programming the stage movements is possible to easily fabricate FBGs with a high degree of customization.

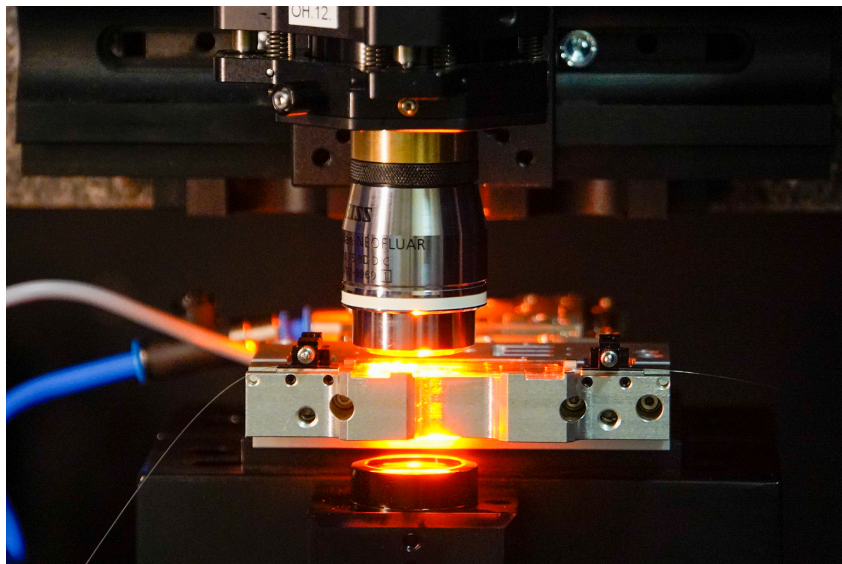


Figure 3.1: Femtosecond laser writing setup.

3.1 SM2000 fiber

The main topic of this part is to analyse the impact of writing FBGs in a fiber where few modes, mainly LP01 and LP11, can propagate in the wavelength range 1500 nm - 1600 nm, pointing out the impact in the resulted spectrum of the overlap integral between the propagating modal field distribution and the written grating.

To satisfy this aspect SM2000 fiber is chosen whose main features are:

- Numerical Aperture (NA) = 0.12
- Core diameter = 11 μm
- Cladding diameter = 125 μm
- Coating diameter = 125 μm
- Cut off wavelength = 1750 nm

As a first step a Matlab script has been coded to simulate and theoretically compute the modal field distribution of the fundamental mode, LP01, and the first higher order mode LP11 which are supposed to propagate in the fiber in the wavelength working range 1500 nm - 1600 nm. The two modal field distribution are respectively shown Fig. 3.2 LP01 mode and Fig. 3.4.

The fundamental mode described in Fig. 3.3 have only one lobe and its maximum is located exactly in the middle of the core fiber so to maximize the overlap integral the grating has to be written in the middle of the fiber core. Furthermore the higher order mode LP11 (Fig. 3.5) presents two lobes and a minimum in the center of the fiber core. As a result of this from a theoretical point of view locating the gratings in a highly precise manner in the middle of the fiber core is possible to maximize the interaction only with the fundamental mode while writing the FBG near the edge core-cladding is maximized the interaction with the LP11 mode.

To demonstrate the correlation between the grating location and the overlap integral previously described, in the same fiber section 3 gratings were written (Fig. 3.6). A first FBG designed to satisfy the phase relation Eq. 3.1 for the fundamental mode (FBG LP01) is located in the center of the core while the other two gratings (FBG LP11) designed to match the condition Eq. 3.1 for the LP11 mode are placed near the edge core-cladding to maximize the interaction according to the theoretical model.

$$\lambda_{\text{Bragg}} = 2\pi \cdot \Delta \tag{3.1}$$

The results are reported in Fig. 3.7 showing the output spectrum of the reflected peaks. According to the theoretical model the higher peaks are the two corresponding to the interaction between FBG_LP11 grating with LP11 mode and FBG_LP01 grating with LP01 mode. while the other two peaks, since the gratings are not interacting with

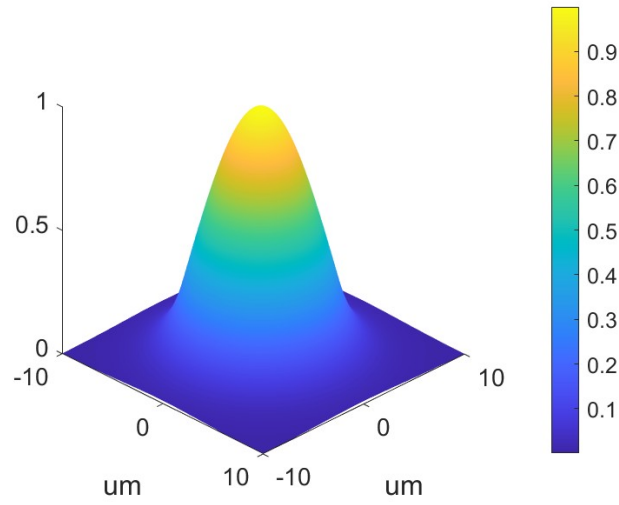


Figure 3.2: LP01 3D modal field distribution.

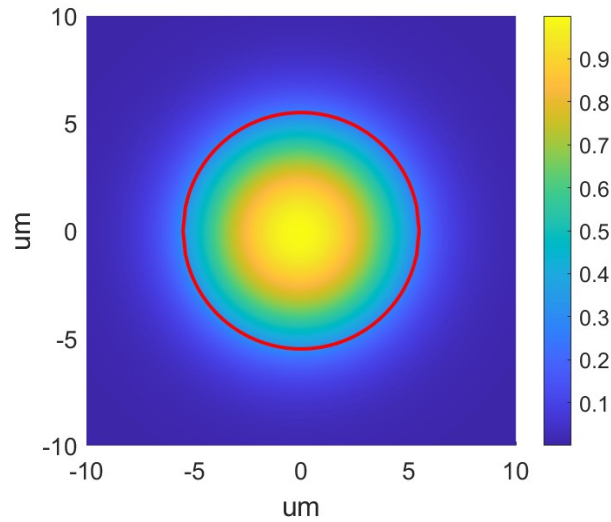


Figure 3.3: LP01 modal field distribution respect to fiber core

the maximum points of the field distributions, are affected by lower reflectivity.

In details the LP11 mode due to its lower neff value respect to LP01 mode interacting with the grating designed for the fundamental mode satisfy the phase relation Eq. 3.1 for a lower wavelength than the designed one. On the other hand the LP01 mode satisfies the "FBG_LP11" grating phase relation for an higher wavelength as correctly reported in Fig. 3.7.

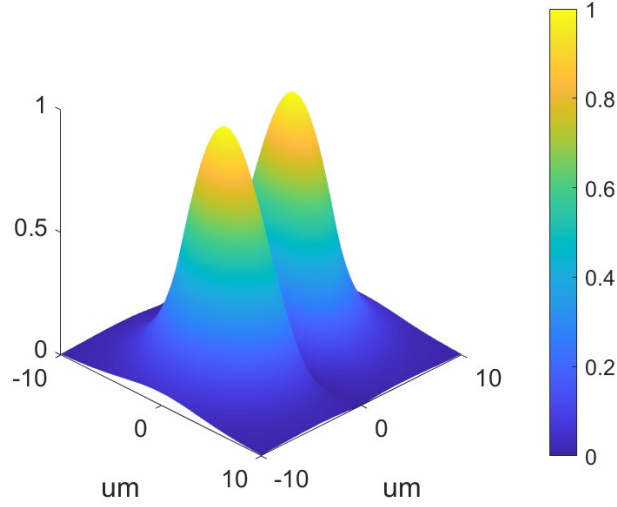


Figure 3.4: LP11 3D modal field distribution.

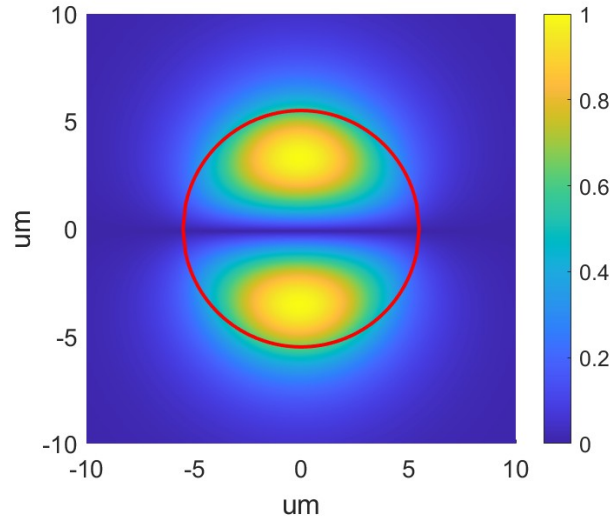


Figure 3.5: LP11 modal field distribution respect to fiber core.

To ensure an high enough excitation of the first higher order mode, according to the theory that the presence of a discontinuity induces the transfer of power from fundamental mode to higher order mode, an offset splice junction was made between the single mode pigtail connected to the source and the SM2000 sample as reported in Fig. 3.9 and Fig. 3.10. In details to prove this the same LP01 mode grating (Fig. 3.8) at first was spliced without any offset to the pigtail source as a result one peak appears in the output spectrum (Fig. 3.9) since only the fundamental was correctly excited. Secondly the previous junction was removed and the FBG was offset spliced to the source pigtail

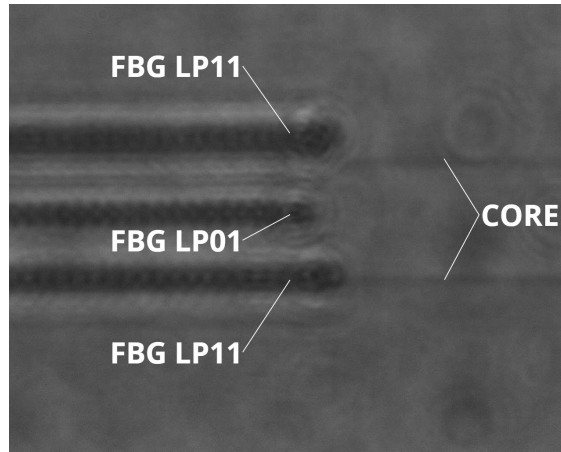


Figure 3.6: Femtosecond laser camera showing the written FBG in two different core position middle and edge core-cladding.

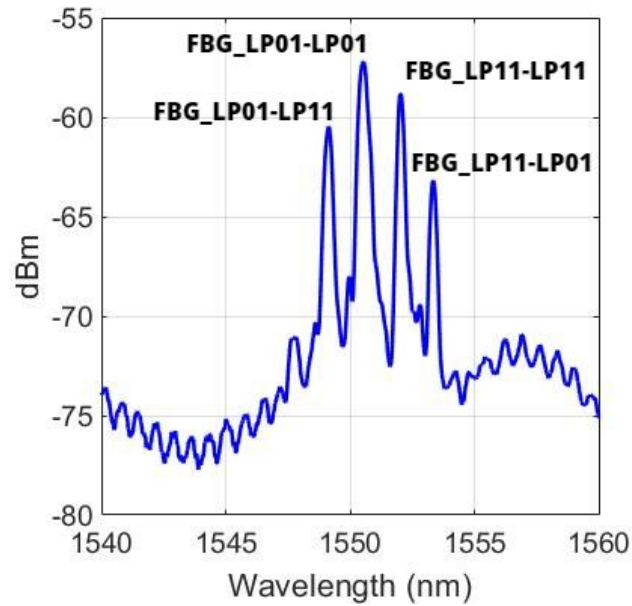


Figure 3.7: Output spectrum showing different peaks whose amplitude depend on the overlap integral between grating and modal field distributions.

to correctly excite both modes. Fig. 3.10 correctly reports now two peaks so the LP11 mode peak appears. Moreover looking at the LP01 mode peak its amplitude results lower than Fig. 3.9 according to the fact that now the source power has to be divided between the two modes.

In addition since the offset splice excites also the higher modes, the FBGs are placed a meter far away from the junction to guarantee that higher modes (LP21 and higher), which cannot propagate in the fiber according to the cut off wavelength value were

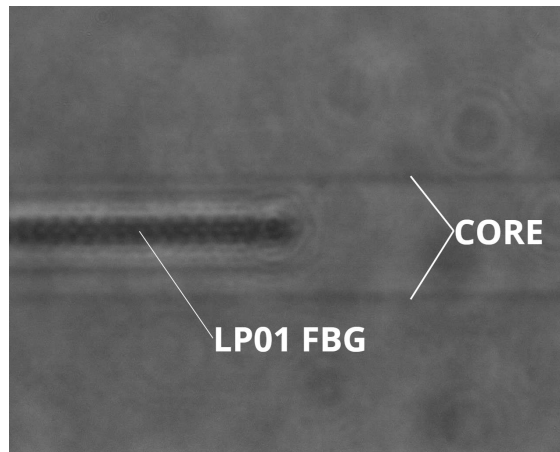


Figure 3.8: Femtosecond laser camera showing FBG LPO1 written in the middle of the fiber core.

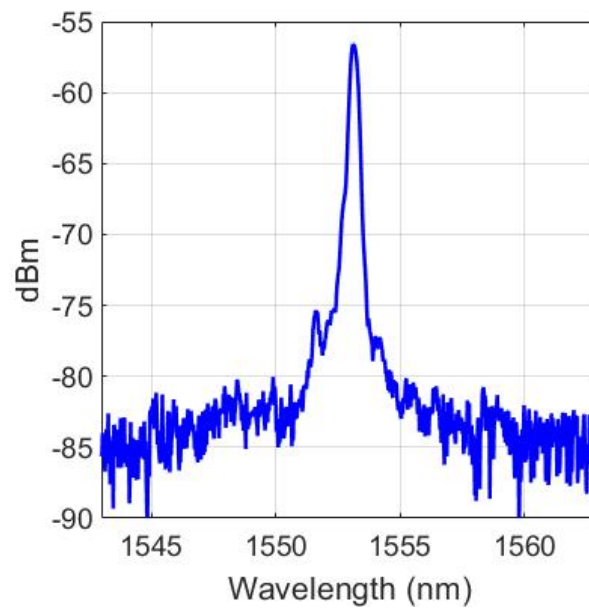


Figure 3.9: Output spectrum of the FBG connected to the pigtail without offset showing only the LP01 mode peak

completed attenuated not affecting the bi-modal behaviour of the fiber. This aspect is clearly pointed out and demonstrated writing a single LP11 mode grating in the edge core cladding (Fig. 3.11) and placing it few centimeters far from the offset slice. The spectrum reported in Fig. 3.12 rightly shown more than two peaks due to the short distance of propagation.

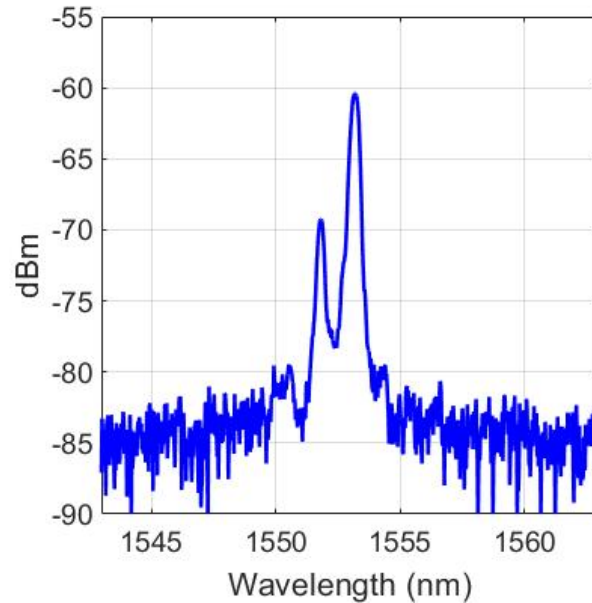


Figure 3.10: Output spectrum of the previous FBG now connected to the pigtail with offset splice showing two peaks LP11 and LP01.

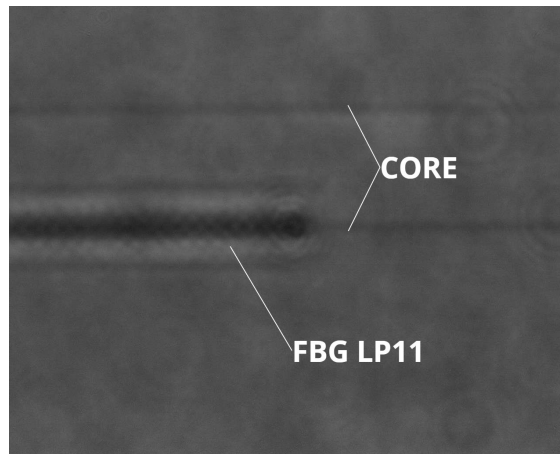


Figure 3.11: Laser camera showing a LP11 mode FBG written in the edge core cladding.

3.1.1 SM2000 fiber: FBG written in the cladding region

The simulations reported in Fig. 3.5 highlight that especially for the LP11 mode looking at the edge core-cladding up to 50 % of the propagating power is distributed in the cladding side so the possibility of writing grating in that area was also investigated.

To do this different LP11 mode FBGs were written progressively increasing the offset between edge core cladding and the beginning of the gratings as shown in Fig. 3.13.

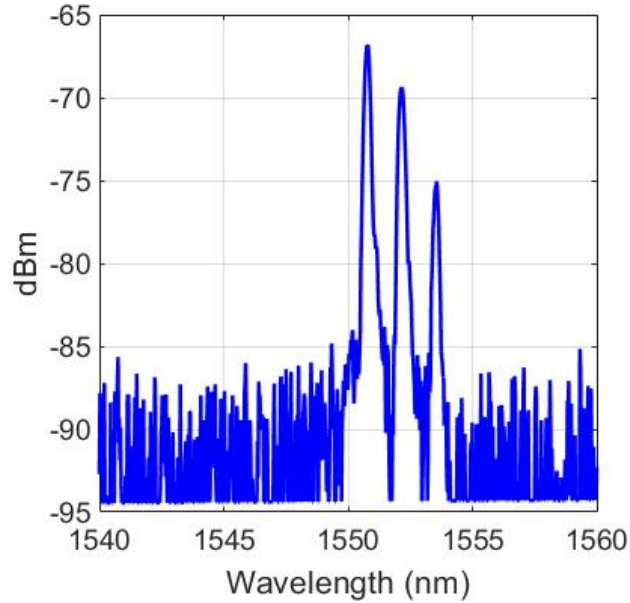


Figure 3.12: Spectrum of a LP11 FBG with no offset connected few centimeters far from an offset splice.

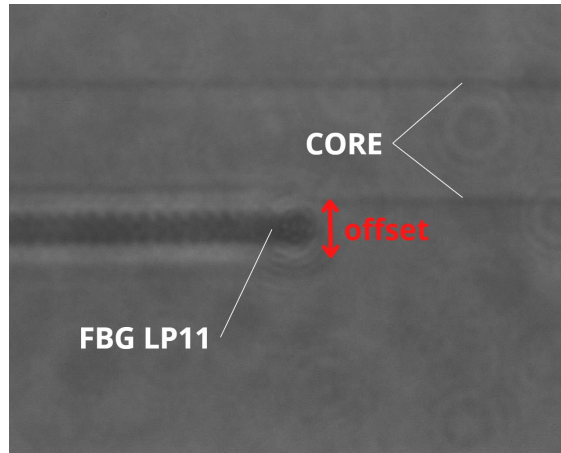


Figure 3.13: Femtosecond laser camera showing the writing scheme of LP11 fbg using offset.

The first step consist in writing the grating with zero offset considering it as a reference (Fig. 3.11) and then the reflected peaks were measured comparing their amplitude which is supposed to reduce as the FBGs are written with greater offset. In details two LP11 mode offset FBGs are realized using respectively $4\ \mu\text{m}$ and $6\ \mu\text{m}$ as offset value and the measured spectra (Fig. 3.12, Fig. 3.14 , Fig. 3.15) correctly shown the peak amplitude reducing with offset up to the limit value, $offset = 6\ \mu\text{m}$ where peaks are no more clearly detected. These results point out the possibility of realizing FBGs also $6\ \mu\text{m}$ above the

upper edge core cladding and $6\ \mu\text{m}$ under the lower edge which is also in agree with the theoretical simulation (Fig. 3.5) showing the LP11 mode whose field distribution completely expires $5\ \mu\text{m}$ - $6\ \mu\text{m}$ far from the edge core cladding.

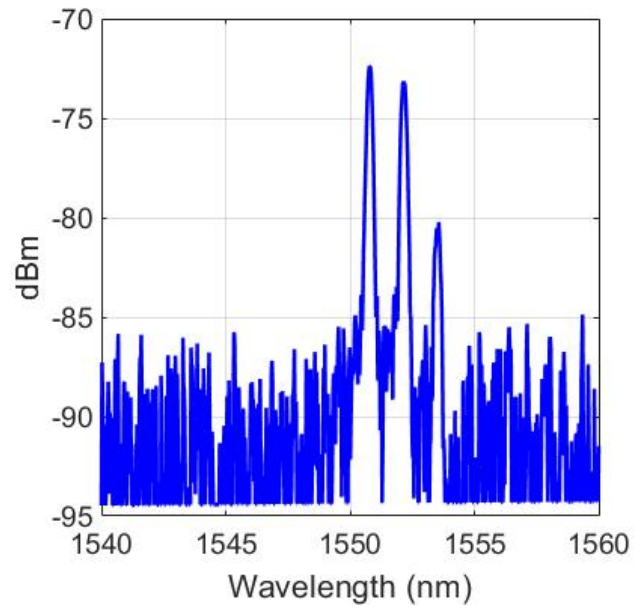


Figure 3.14: Spectrum of a FBG written $4\ \mu\text{m}$ offset from edge core cladding.

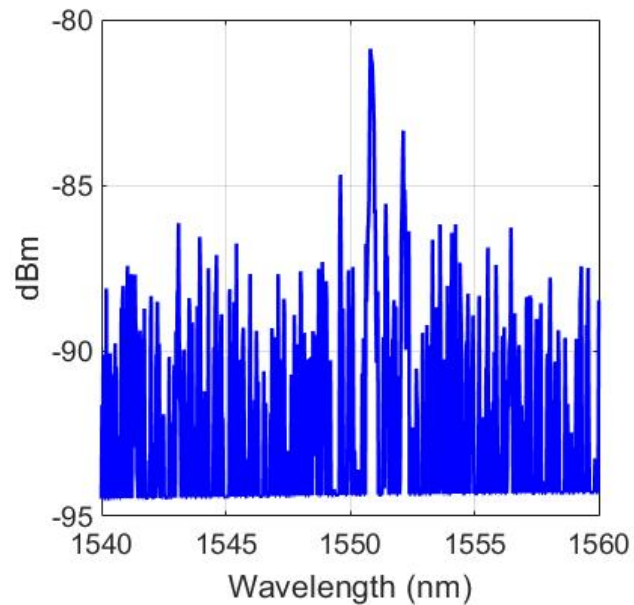


Figure 3.15: Spectrum of a FBG written $6\ \mu\text{m}$ offset from edge core cladding.

3.1.2 SM2000 fiber: sensing unit combining FBG and SMS

The results presented in the previous subsections in a first phase are useful in confirming the modal field distribution analysis knowing better how the propagating field is distributed in the fiber. However, as main important aspect, they allow and improve the development of a novel sensing unit which combines in the same fiber a FBG and an in-line interferometer (SMS) made by offset splicing a few modes SM2000 fiber section between two single mode pigtail.

The reflected output spectrum is report Fig. 3.16 where is clearly shown the bi-modal interferometric patten between LP01 and LP11 mode due to their different phase velocity plus the FBG peaks of the two propagating modes which have the features previously described such as the higher amplitude of LP01 peak since only the LP01 grating was written in the middle of the core similarly to the case described in Fig. 3.8

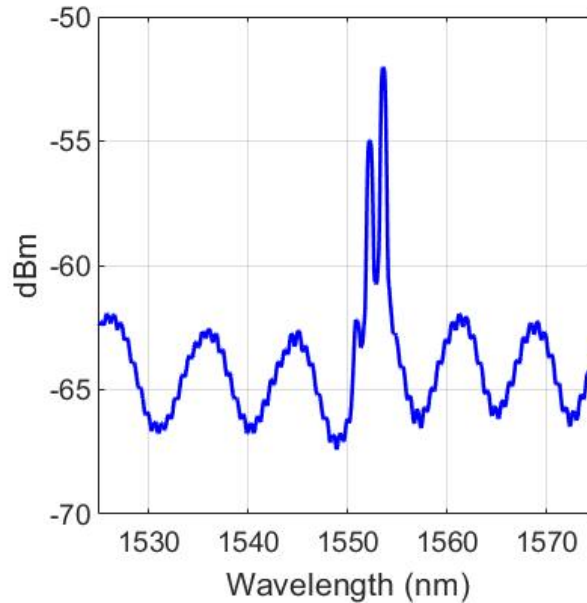


Figure 3.16: Spectrum of the sensing unit combining FBG and SMS.

This sensing structure shows an efficiently feature to reduce multiple physical quantities cross sensitivity especially between temperature and strain which is a very challenging issue limiting several sensing solutions. In fact interferometric sensors have red shift to temperature and blue shift to strain while FBGs exhibits in both cases a red shift [20]. Moreover considering temperature measurements SMS and FBG show different sensitivity respectively up to 100 pm/°C and 10 pm/°C allowing post processing cross sensitivity compensation.

3.2 Bend insensitive fiber (BIF)

The aim of this particular section is to elucidate the process of embedding a Fiber Bragg Grating (FBG) in a bend-insensitive fiber, with the ultimate goal of exploiting the unique properties of the fiber to produce a highly efficient sensing unit. By directly writing through the coating of the fiber, it becomes possible to create a sensing unit that is impervious to bend losses and other forms of disturbances that could interfere with the accuracy of the measurement.

The successful combination of FBGs with bend-insensitive fibers in the construction of sensing units provides a novel and highly effective solution to the challenge of mitigating bend losses and other disturbances. This approach enables the creation of sensors that are both reliable and accurate, while remaining immune to the effects of electromagnetic interferences like common dielectric fibers. The result is a sensing unit that is capable of providing highly precise and reliable measurements even in challenging conditions, making it an indispensable tool for a wide range of scientific and industrial applications.

These fibers possess a remarkable ability to maintain their optical integrity even when subjected to tight bends; in details the used fiber (G657 A2 BIF) can reject bend losses thanks to a specific modulation of the refractive index profile forming a trench with relatively low refractive index around the fiber core as shown in Fig. 3.17.

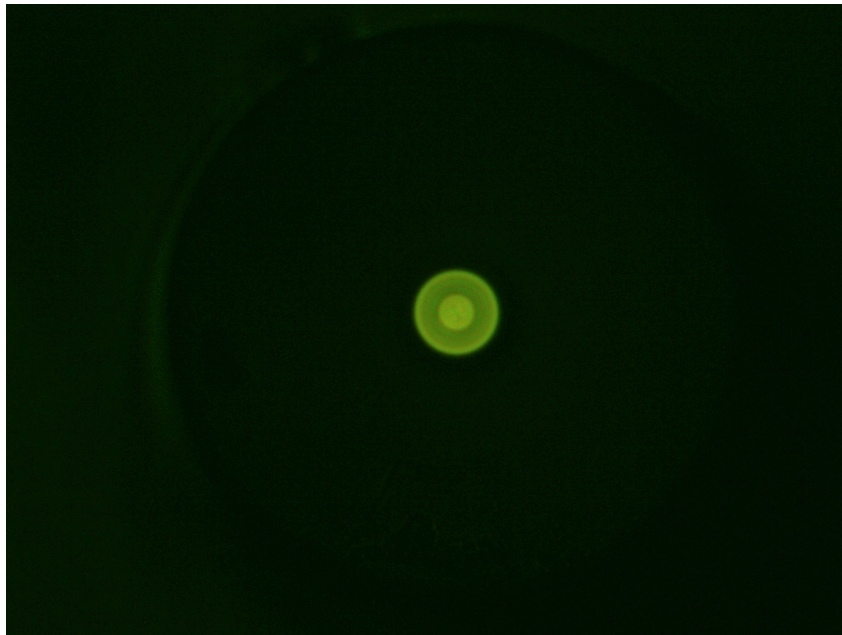


Figure 3.17: BIF G657A2 analysed using microscope.

In order to gain a more comprehensive understanding of the physical structure of the fiber, it was deemed necessary to undertake a preliminary step. Despite the information available on the fiber's data-sheet, there remained some ambiguity surrounding the fiber's

physical dimensions and structure. To address this issue, a microscopic analysis of the fiber in a vertical section was conducted.

This analysis provided valuable insights into the physical characteristics of the fiber, particularly with regard to the diameter of the core and cladding layers. The trench section, which is not always fully described in the data-sheet, was also thoroughly examined during the analysis. This additional information proved to be essential in developing a more accurate understanding of the fiber's structure and physical properties. The use of microscopy in this investigation allowed for a detailed examination of the fiber's structure at a high level of magnification, providing a greater level of insight than would be possible through visual inspection alone. By gaining a deeper understanding of the fiber's physical properties and structure, it is now possible to more accurately model and predict its behavior in a range of different applications.

Overall, this preliminary step has proven to be an important and valuable part of the investigation into the fiber's physical properties. It has allowed for a more comprehensive understanding of the fiber's structure and characteristics, and has provided a solid foundation for further analysis and experimentation.

The obtained measurements are.

- Cladding diameter $\simeq 125.60 \mu\text{m}$ (Fig. 3.18)
- Core diameter $\simeq 8.28 \mu\text{m}$ (Fig. 3.19)
- trench diameter $\simeq 18.74 \mu\text{m}$ (Fig. 3.20)

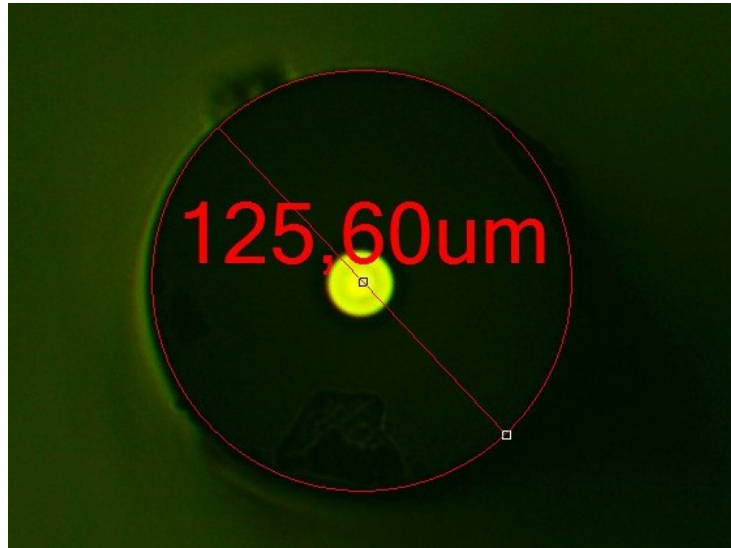


Figure 3.18: BIF cladding diameter measured using microscope.

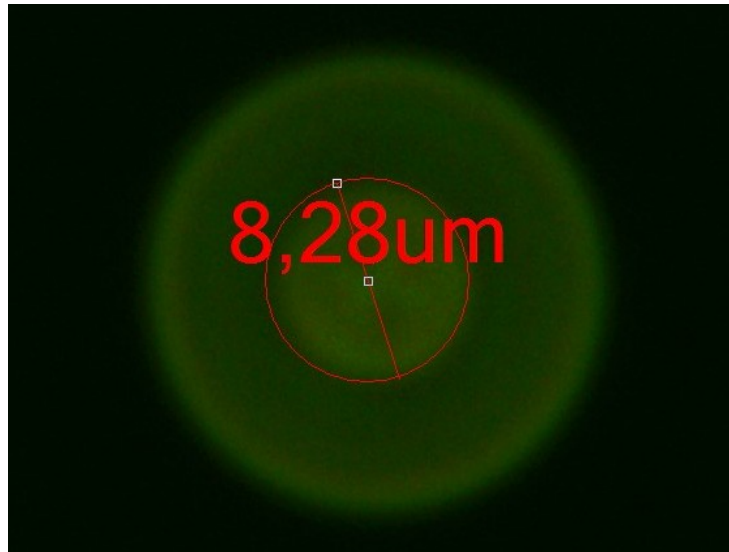


Figure 3.19: BIF core diameter measured using microscope.

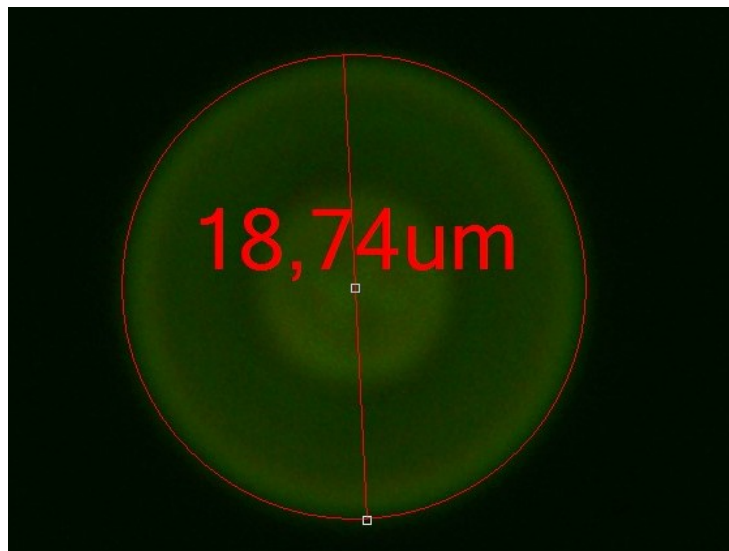


Figure 3.20: BIF trench diameter measured using microscope.

Once the approximate physical structure of the fiber had been established, the fiber was loaded into the Femtosecond laser for the fabrication process . To ensure accurate alignment of the laser's focused spot with the fiber core, the stage holding the fiber was carefully adjusted using the axes control software which provides micro movement in a highly precise manner. However, this step was found to be more complex than for standard telecommunication fibers due to the presence of a dark coating which made the core difficult to detect using the laser camera, as depicted in Fig. 3.21

To overcome the issue of the dark coating during the fiber Bragg gratings fabrication, it is important to program the camera settings appropriately (Fig. 3.22). In particular, the settings must be able to compensate for the dark coating so that the core and trench profile can be easily detected. By doing so, it is possible to optimally focus the core section of the fiber, which is critical for the success of the fabrication process. To ensure that the fiber is correctly focused, it is necessary to measure the values of the core, cladding, and trench diameter using a microscope, or check them in the data sheet if available, as well as to confirm these values using a laser camera. The laser camera is an important tool for verifying the accuracy of these parameters, as it provides a more precise and accurate image of the fiber structure. Once the core is correctly focused, it is then possible to select the start-position and end position of the gratings and enable the fabrication process. The start and end positions are important parameters in the fabrication process, as they determine the length and the location of the gratings respect to the fiber core.

Overall, the appropriate programming of camera settings, accurate measurement of fiber dimensions, and precise selection of start and end positions are crucial for the successful fabrication of FBGs. By following these steps, it is possible to produce high-quality FBGs with the desired characteristics, in this specific case the bend insensitive feature, for various applications in sensing systems.

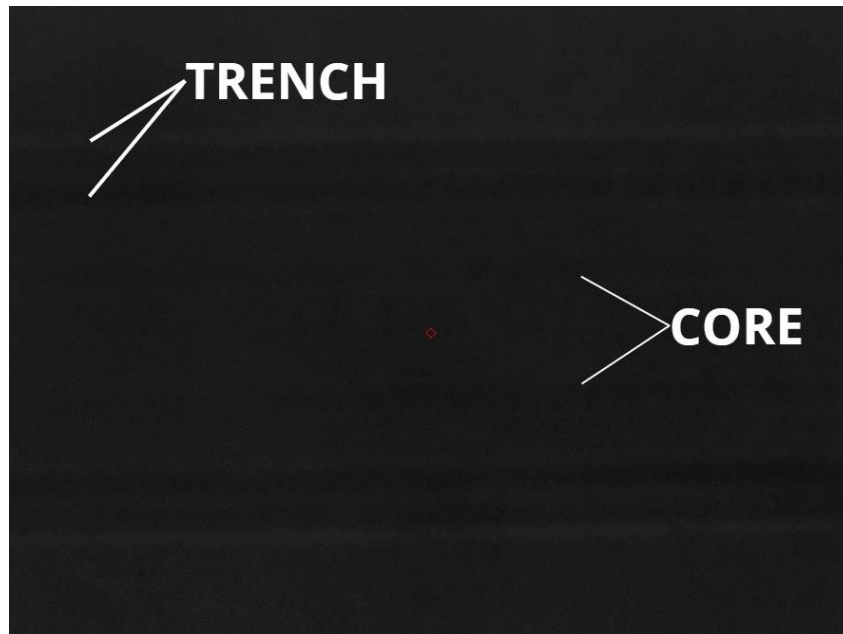


Figure 3.21: Femtosecond-laser camera focused on fiber core no optimized case.

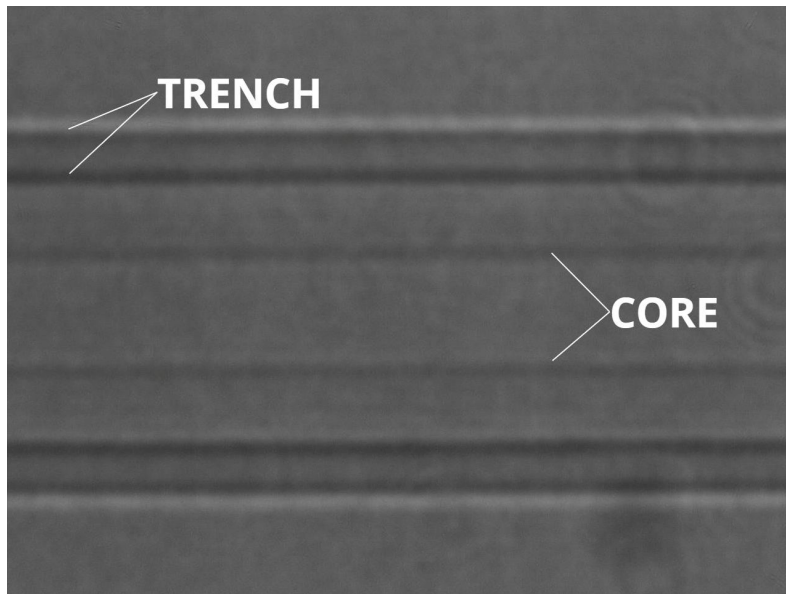


Figure 3.22: Femtosecond-laser camera focused on fiber core optimized case.

Fig. 3.23 shows the output result at the end of the fabrication process. Since the correctness of previous steps the emitted pulsed light, whose power was previously optimized, when the stage moves between the two grating extremes, is exactly focused only in the desired section of the core provoking the periodic index modulation according to the desired wavelength in this specific case $\lambda_{Bragg} = 1550$ nm.

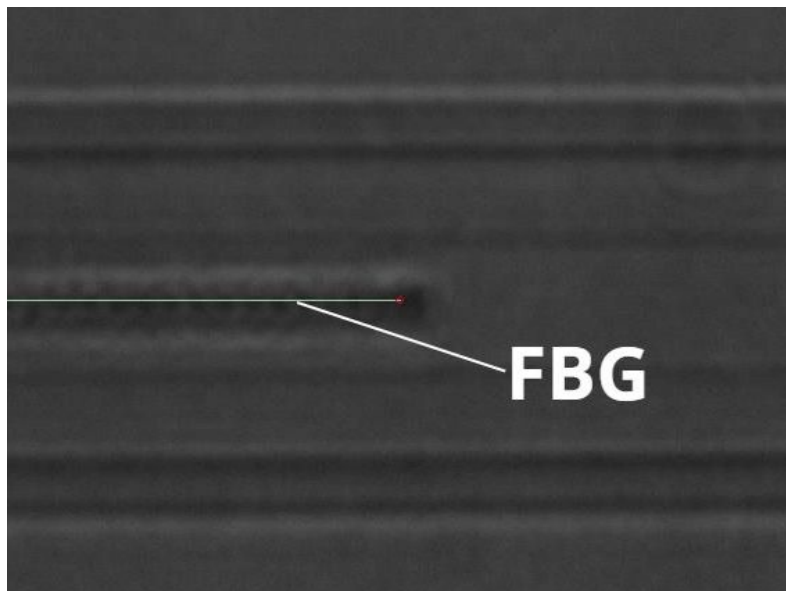


Figure 3.23: Femtosecond-laser camera showing a written grating.

The output spectra reported in Fig. 3.24 is measured in reflection using an optical circulator optimized in the wavelength range 1500 nm-1600 nm, a *KOHERAS superK* source and a *HP70951A* optical spectrum analyzer with resolution bandwidth set to 1 nm. Since the measured wavelength peak is $\simeq \lambda_{Bragg} = 1550$ nm, the correctness of the entire fabrication process is guaranteed.

Future improvement may be linked to increase peak reflection, reduce side-lobes, adjust the n_{eff} value for a given wavelength to fit λ_{Bragg} constraints in a better way.

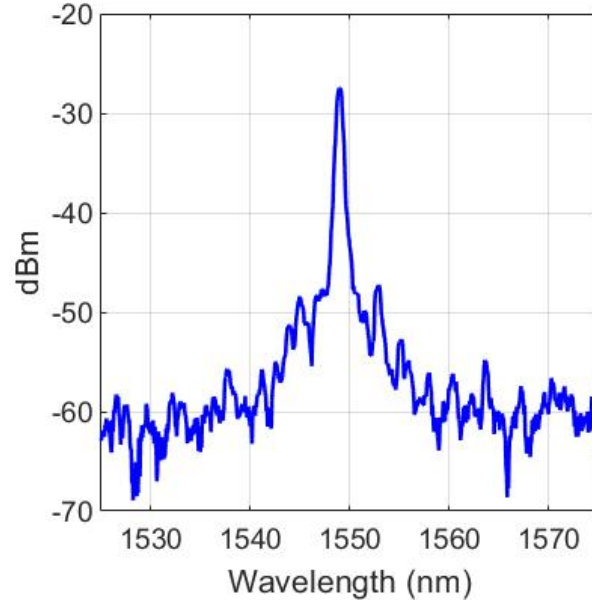


Figure 3.24: FBG 1550 nm spectrum.

3.3 Polyamide coated fiber for high temperature FBGs

Real-time monitoring is crucial in various industrial applications, such as chemical plants, power plants, and oil and gas refineries, where safety and efficiency are critical. However, real-time monitoring systems often face challenges in environments with high temperatures, which can compromise the performance and lifespan of common sensing solutions. To overcome this challenge, researchers have investigated the use of fiber Bragg gratings (FBGs) with a polyamide coating, which can withstand high temperatures.

Polyamide coatings offer significant advantages over more common silicate coatings. Specifically, polyamide coatings exhibit a higher tolerance to temperatures above 100 °C, making them ideal for use in high-temperature environments. This enhanced tolerance allows FBGs with polyamide coatings to operate more efficiently and have a longer lifespan than those with silicate coatings. The resulting FBGs are highly sensitive to temperature changes and can be used to measure temperature in real-time making them ideal for use in monitoring systems, especially where rapid, accurate data collection is essential.

In details the fiber used to realize the FBGs is the *Thorlabs SM1550P Polyimide-Coated Single Mode Fiber* whose main features are:

- Numerical Aperture (NA) = 0.12
- Core diameter = 9 μm
- Cladding diameter = 125 μm
- Polyamide coating diameter = 145 μm
- Cut off wavelength = 1260 nm

To evaluate the quality of the written grating a commercial polyamide FBG was used as a reference. Fig. 3.25 shows the reflected peak and the measurement is obtained using a resolution bandwidth equal to 0.1 nm and a span of 10 nm from 1549 nm to 1559 nm.

The main features of the reflected spectrum which are considered as standard reference are the following:

- Full width at -3 dB equal to 400 pm
- Side lobes attenuation between peak and side lobes higher than 20 dB.

The FBGs which are directly fabricated using the femtosecond laser are measured in the same condition of the commercial gratings and the results are reported in the Fig. 3.26 for sample 1 and Fig. 3.27 for sample 2 showing also the repeatability of the fabrication process whose main features are:

- Full width at -3 dB equal to 400 pm
- Side lobes attenuation between peak and side lobes higher than 12 dB.

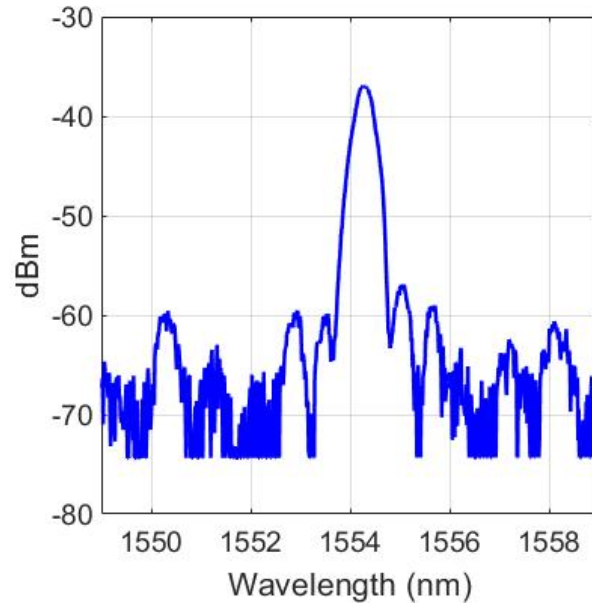


Figure 3.25: Commercial polyamide FBG.

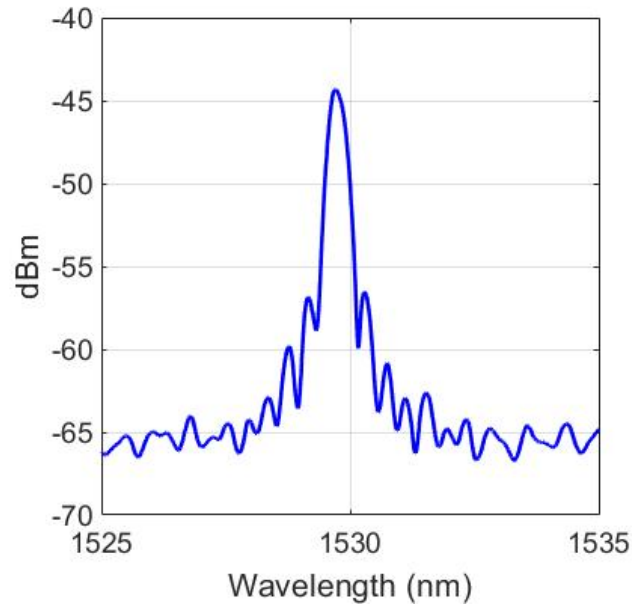


Figure 3.26: Spectrum of polyamide FBG 1 written using Femtosecond laser.

The results perfectly match the commercial reference on the full width at -3 dB while the constrain about the sidelobe attenuation was not so easy to achieve and it represents a challenging topic for future analysis.

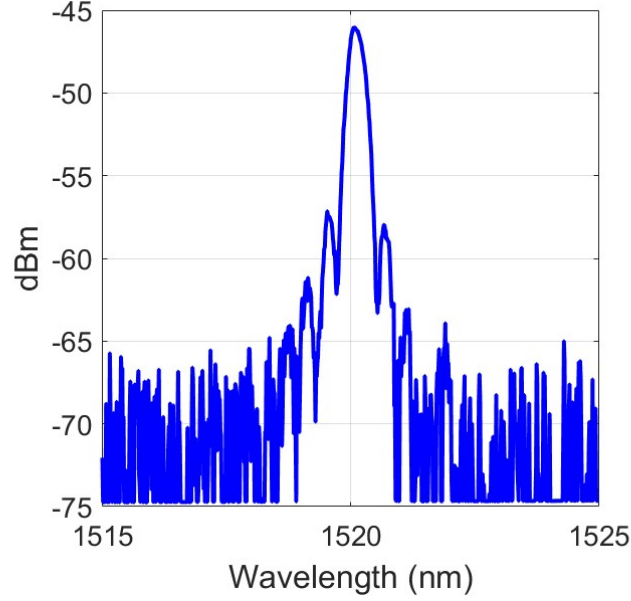


Figure 3.27: Spectrum of polyamide FBG 2 highlighting the fabrication repeatability.

A second optimization step is related to the computation of the effective refractive index (n_{eff}) value, which is a fundamental parameters in obtaining the reflected peak exactly at the desired wavelength compensating the chromatic dispersion effects.

To do this a preliminary phase is requested: in a test fiber sample several FBGs has been written for different wavelengths in the desired range mainly 1500 nm-1600 nm using a common n_{eff} value equal to 1.4472. According to Eq. 3.2 the femtosecond laser induce in the core a periodic index modulation whose pitch is equal to Δ .

$$\Delta = \frac{2\pi \cdot n_{eff}}{\lambda_{Project}} \quad (3.2)$$

Then using a optical spectrum analyzer with resolution bandwidth higher than 0.1 nm the gratings are analyzed measuring the peak wavelength (λ_{Peak}). Once these steps are done knowing the value of Δ previously computed is possible to invert the relation Eq. 3.2 obtaining Eq. 3.3 which allows to compute a good approximation of the n_{eff} for any desired wavelength.

$$n_{eff} = \frac{\Delta \cdot \lambda_{Peak}}{2\pi} \quad (3.3)$$

In conclusion since through the writing of a single test grating is possible to estimate quiet well the n_{eff} for the next fabrications, the shown method works quiet well resulting in a valid solution in particular with fiber whose n_{eff} is not clearly defined in the data-sheet or difficult to computed with theory, moreover it is a effective manner to prove and

validate the theoretical model based on Bessel-equation often used to estimate the n_{eff} values.

The analysis done on the variation of the n_{eff} with wavelength are shown in Fig. 3.28 where the computed values of n_{eff} for different wavelengths are interpolated with a first order polynomial using the Matlab function Polyfit. The shown results correctly match the theoretical models in fact the n_{eff} as expected decreases for higher wavelengths enhancing the validation of this empirical solution to estimate the n_{eff} .

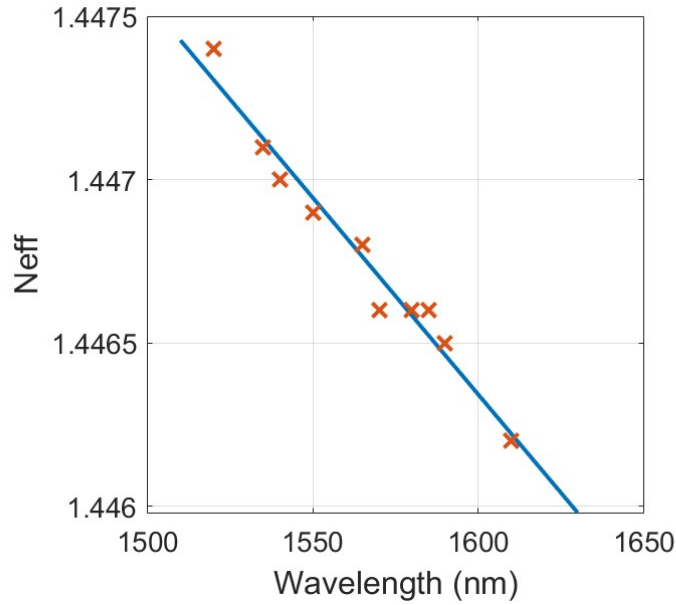


Figure 3.28: Interpolation of points representing the computed n_{eff} values for different wavelengths.

In details the values are reported in Tab.3.1

Lambda_project (nm)	Lambda_peak (nm)	Neff
1520	1520.12	1.4474
1535	1534.82	1.4471
1540	1539.69	1.4470
1550	1549.59	1.4469
1565	1564.41	1.4468
1570	1569.19	1.4466
1580	1579.23	1.4466
1585	1584.20	1.4466
1590	1589.09	1.4465
1610	1608.76	1.4462

Table 3.1: Polyamide fiber n_{eff} values versus wavelength

3.4 SFM28 fiber

In this section the goal is to realize fbgs in the most widely used standard telecommunication fiber to realize practical sensing unit merging the main features of fiber optic sensor with the cost effective price of SFM fibers due to their large diffusion in telecommunication market.

The used fiber is *Corning SFM28 TM* whose main features are the following:

- Numerical Aperture (NA) = 0.14
- Core diameter = 8.2 μm
- Cladding diameter = 125 μm
- Coating diameter = 250 μm
- Cut off wavelength = 1260 nm

As explain before the idea for obtaining cost effective FBGs is to use a fiber which is a good trade off between performances and price in details from one hand due to the large diffusion is possible to use also simpler and cheaper laboratory instruments such as cleaver, splicer, stripper etc.. while on the other hand this fiber badly suffers high temperature over 70 °C- 80 °C limiting the sensing range and the application fields. Moreover its measured spectral response may be altered by bend loss reducing the overall performance of the sensor.

A further limit of this fiber, directly linked to the femtosecond laser fabrication process is the reduced capability in supporting the pulsed emitted light by the writing tool. Indeed to avoid critical damages in the core increasing the losses and compromising the grating realization, high attention has to be paid in well optimizing the emitted light which must be kept at low level during all the writing process.

3.4.1 Most common errors in writing gratings

Since the low cost of this fiber it is been possible to perform a large number of experiments varying all the main important fabrication parameters such as emitted power, grating length, stage movement velocity etc.. highlighting their impact on the grating measured spectrum to better know how the process works in order to minimize the errors during future grating realization in high performance sensing designed fibers.

At first before any writing procedure to avoid preliminary errors the sample setup should be tested verifying the correct capability in focusing the edge core cladding and the pulse absorption behaviour which in normal condition should provoke a circular dot without any astigmatic distortion as shown in Fig. 3.29

The most common error in realizing FBGs is linked to the management of the emitted power by the laser which has to induce the periodic index modulation in the core fiber.

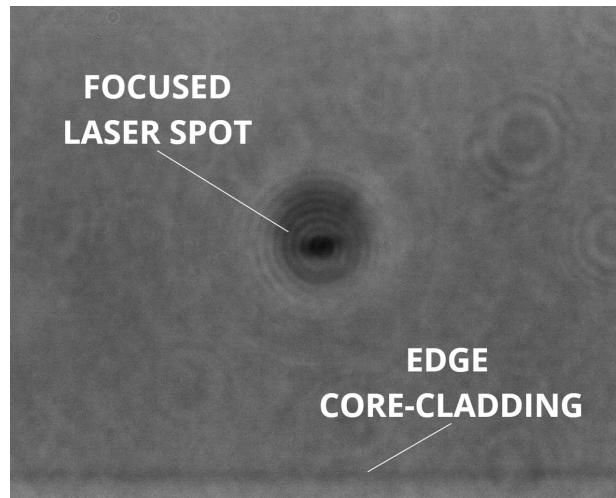


Figure 3.29: Laser camera showing a correct focused laser spot without any astigmatic distortions.

Excluding the two extremes cases of too low power so any modulation is induced and too high power where only losses are made (Fig. 3.30), many times may happen that the measured spectra has the shape similar to Fig. 3.31. In this case since the grating peaks clearly appears the emitted power is only slightly too high, however this induces too high side lobes provoking disturbances which lead to zero the applicability possibilities of this FBG as sensing unit.

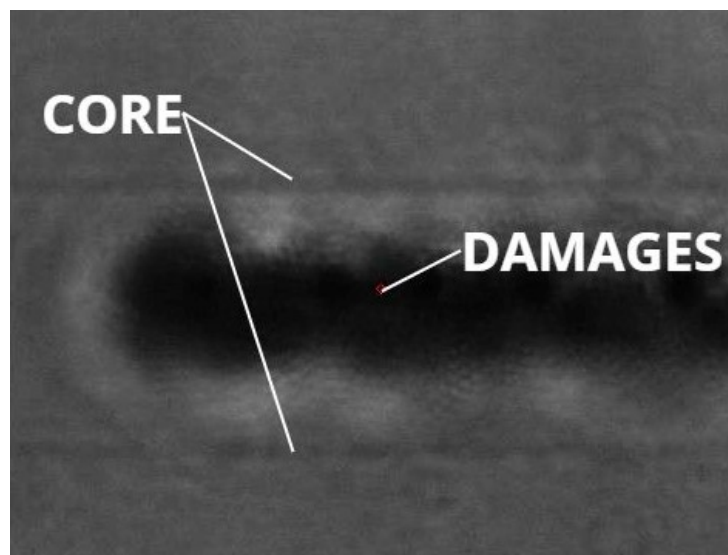


Figure 3.30: Laser camera showing a FBG written using too high emitted power.

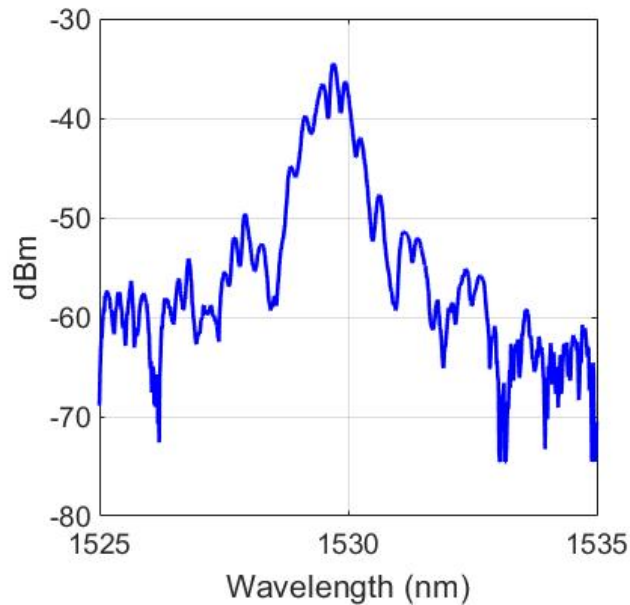


Figure 3.31: Spectrum of a FBG written using too high emitted power.

Another important parameter limiting the grating realization although the emitted power has been correctly set, is the planning of the stage velocity and its trajectory. In fact since the pulses are emitted regularly the quantity of the absorbed power in a given core section depends on the exposure time which is defined by the stage velocity. Not to generate areas with higher exposure the grating extremes should be selected in the coordinates where the stage has completed its acceleration or deceleration phases assuming a constant velocity as described in Fig. 3.32

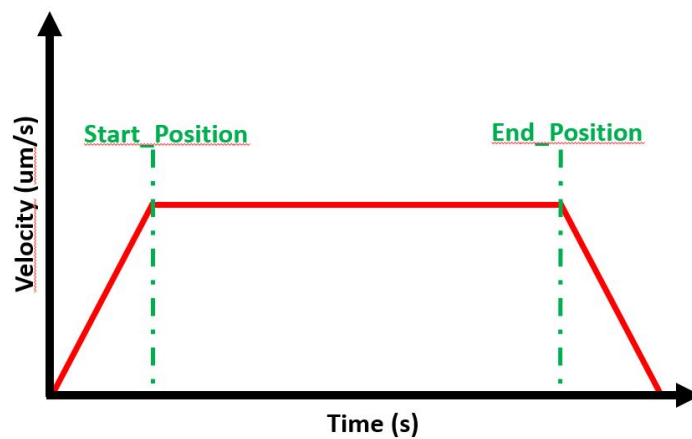


Figure 3.32: Schematic of a correct grating extremes selection respect to the stage trajectory.

The effects of selecting the end_position in a section where the stage is in a deceleration phase are reported in Fig. 3.33 showing a periodic index modulation correctly written in the left part of the pictures since the stage moves at constant speed while the right part presents a large dark area indicated the higher absorbed power causing losses and a measured spectrum with compromised shape (Fig. 3.34)

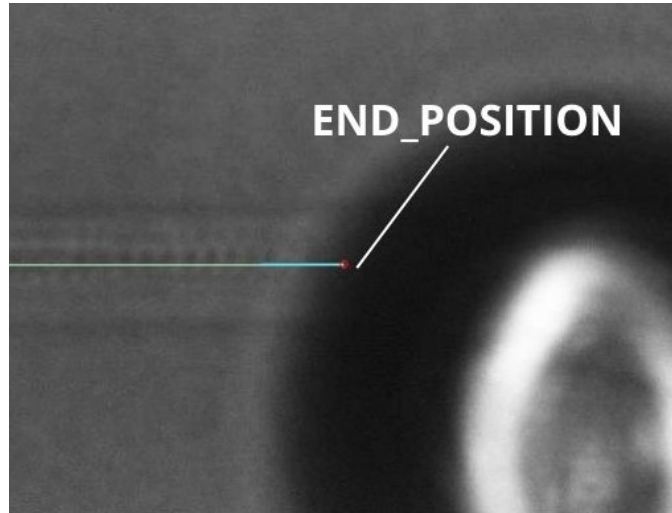


Figure 3.33: Laser camera showing a written FBG whose end_position is located in the deceleration phase.

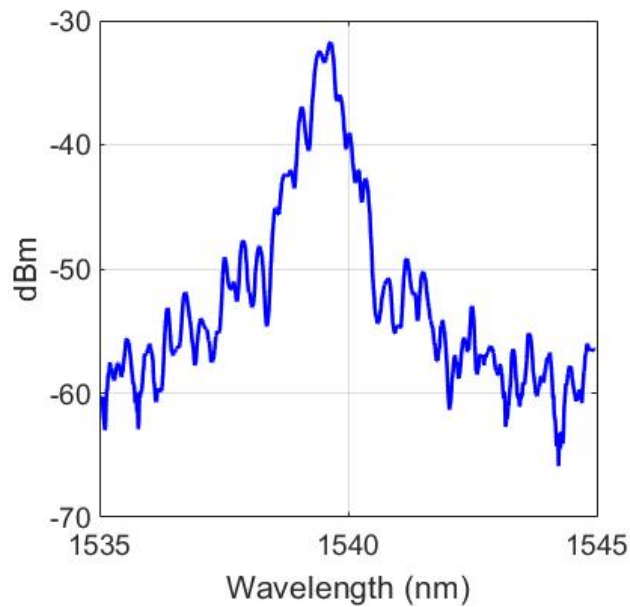


Figure 3.34: Measured reflected FBG spectrum with too much noise due to errors in moving the stage.

3.4.2 SFM-28 FBG optimized realization process

If no one of the previous described errors happen the correct steps are respectively reported in Fig. 3.35 showing the end_position of the gratings correctly terminated without any area with higher absorbed power. Fig. 3.36 reports a well optimized emitted power inducing the periodic index modulation with contained losses which works as a narrow band reflector as theoretically expected. The output spectrum measured in reflection is shown in Fig. 3.37

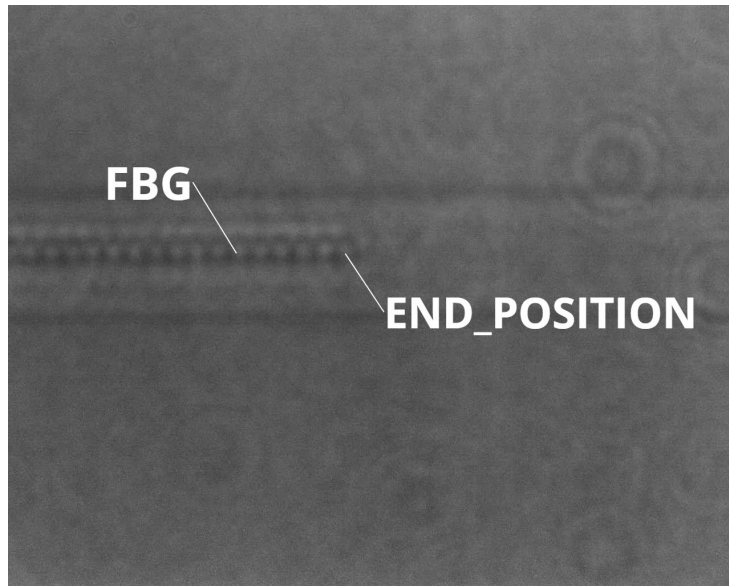


Figure 3.35: Laser camera showing a written FBG whose end_position is correctly located in the constant velocity phase.

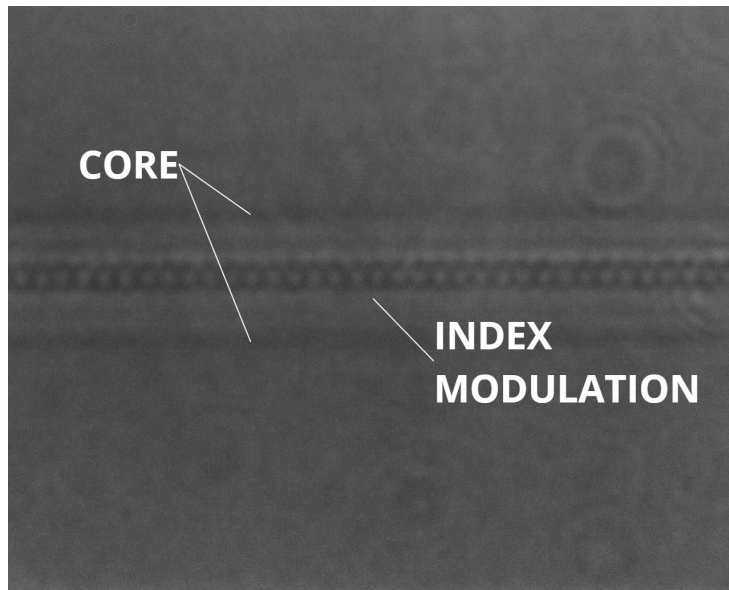


Figure 3.36: Laser camera showing the induced periodic refractive index modulation.

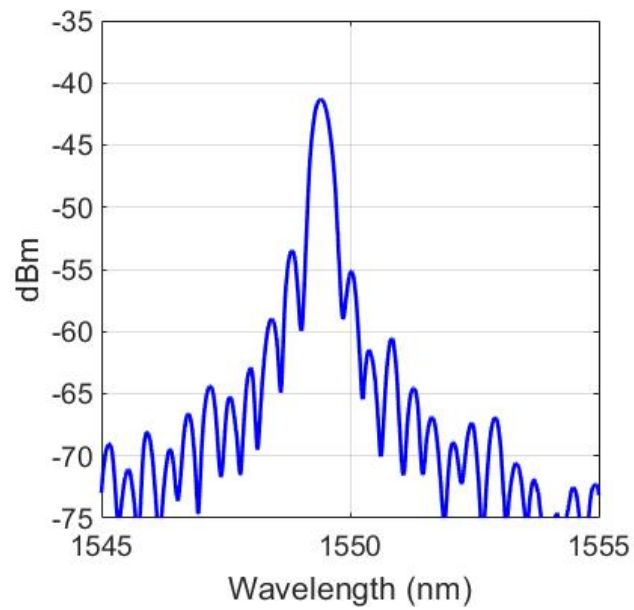


Figure 3.37: Measured reflected spectrum of a FBG written using the optimized fabrication process.

3.5 SFM-28 FBG practical implementation as single point temperature sensor

In this section it is presented a possible practical application of the grating as a single point temperature sensor to monitor, test and validate the thermal properties of graphite based chemical compounds when they interact with a laser acting as a heating source (Fig. 3.38)

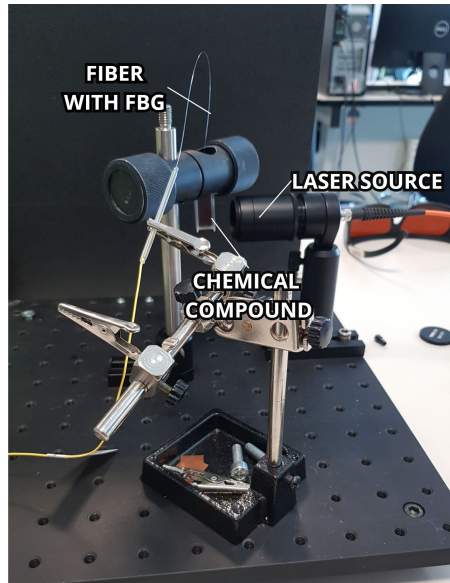


Figure 3.38: Setup used to optically heat and test chemical compounds.

The benefits of using a FBG as sensor unit in these contexts are strictly related to its extreme small size which can be easily embedded directly in the test tube, moreover the completely dielectric structure, not requiring a power source, guarantees the impossibility of causing fire a really appreciate feature in case of unstable or inflammable compounds. Last but not least the absence of metallic components since they can became hot absorbing the optical power emitted by the laser source, ensure a good accuracy in the temperature measurements and also a strong rejection to corrosion.

The experimental results are presented in Fig. 3.39 where using a fixed emitted optical power the thermal effects are evaluated looking at the λ_{Bragg} shift of the grating in three different cases. At first using water as a reference that shows as expected very small shift secondly illuminating two graphite based compounds which shows a significant shift due to their enhanced thermal properties.

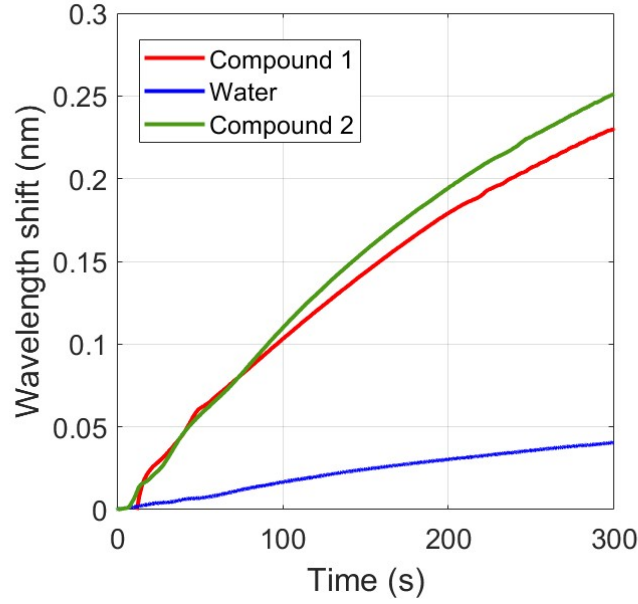


Figure 3.39: Measured wavelength shift due to laser heating for different graphite based compounds respect to water.

3.6 SFM-28 FBG practical implementation as multi points array temperature sensor

In this section a smart multi-point sensing solution to monitor temperature with high accuracy is presented. The sensor structure shown in Fig. 3.40 is characterized by 13 2 mm long FBGs spatially spaced following a custom density scheme 8 mm for the 2 gratings located at both extremes and 3 mm for the FBGs in the middle section of the fiber obtaining a compact embeddable sensor able to monitor in real time heat-map and temperature profile

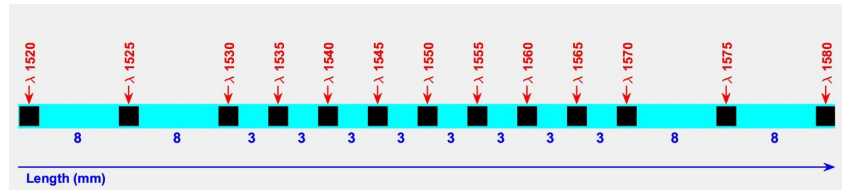


Figure 3.40: Schematic of the 13 point FBG sensing array used as distribute temperature sensor.

The chosen λ_{Bragg} , whose reflected spectrum is reported in Fig. 3.41, are respectively shift by 5 nm from each other in the range 1520 nm - 1580 nm avoiding undesired overlap between two adjacent peaks during the temperature monitoring activity. Since the supposed thermal sensitivity is equal to 10 pm/°C the overlap condition between two peaks

can happen only for a temperature higher than 500 °C which is well beyond the maximum temperature supported by the sensor.

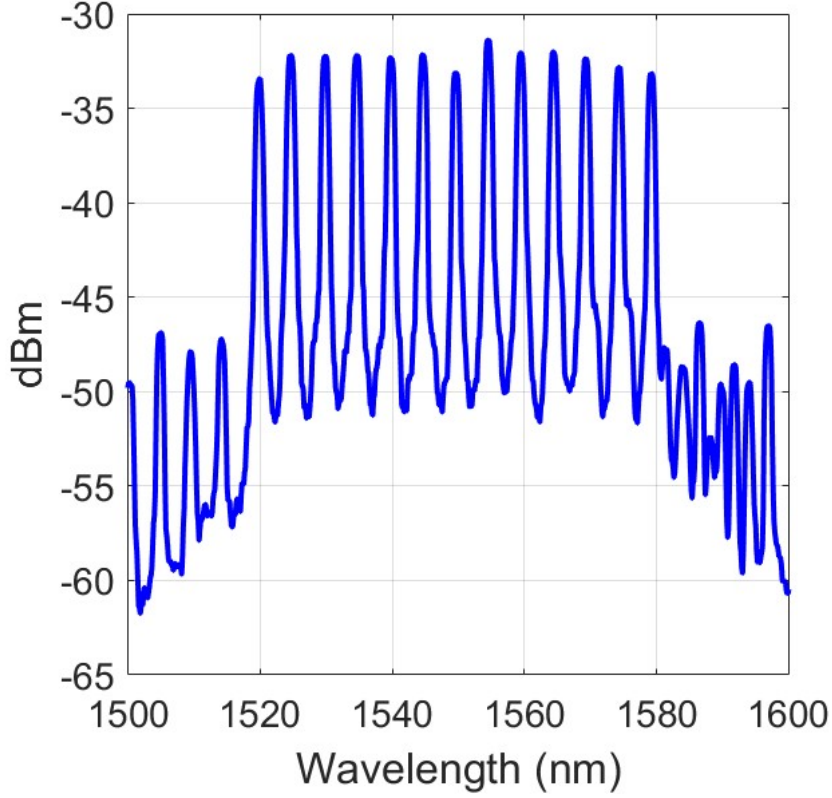


Figure 3.41: Measured reflected spectrum of the 13 point FBG sensing array.

To better satisfy the constrain in respecting the λ_{Bragg} for all the peaks with the same accuracy, the variation of the n_{eff} values with wavelength is also analysed as done for the polyamide fiber. The results are reported in Fig. 3.42 and in Tab. 3.2

Furthermore to consolidate the fabrication process of this sensing unit evaluating its repeatability 9 samples has been made and analysed in the same way. Fig. 3.43 shows the coefficient of the first order polynomial which interpolates the averaged n_{eff} values considering all the 9 sensors.

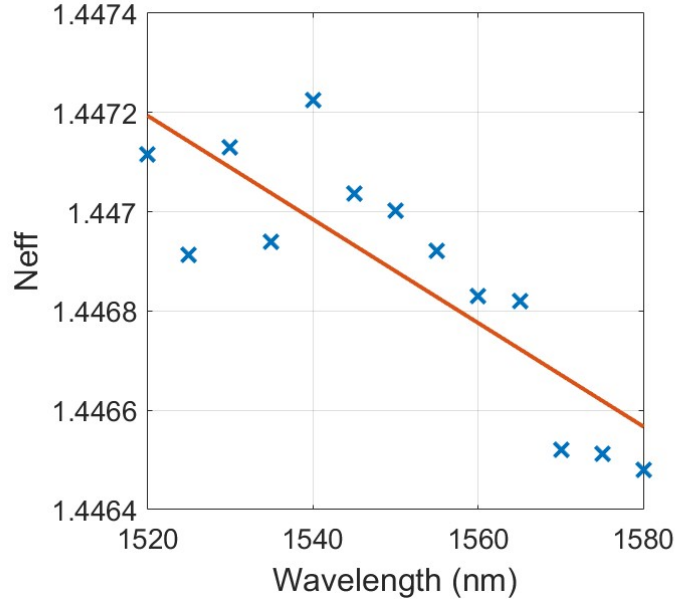


Figure 3.42: First order polynomial interpolation highlighting the variation of n_{eff} for different wavelength values.

Lambda_project (nm)	neff_project	Lambda_peak (nm)	Neff	Error (nm)
1520	1.4473	1519.80	1.4471	0.20
1525	1.4473	1524.59	1.4469	0.41
1530	1.4473	1529.81	1.4471	0.19
1535	1.4473	1534.61	1.4469	0.38
1540	1.4473	1539.91	1.4472	0.08
1545	1.4473	1544.71	1.4470	0.28
1550	1.4473	1549.68	1.4470	0.32
1555	1.4473	1554.59	1.4469	0.41
1560	1.4473	1559.49	1.4468	0.51
1565	1.4473	1564.48	1.4468	0.52
1570	1.4473	1569.15	1.4465	0.85
1575	1.4473	1574.14	1.4465	0.86
1580	1.4473	1579.10	1.4464	0.89

Table 3.2: Measured peaks of 13 points FBG sensing array.

This sensing array has been used to measure the temperature variation during a simulation of laser tumor ablation showing encouraging results in detecting which areas of biological tissues have been injured most by the laser ablation due to the higher increment of temperature. Fig. 3.44 shows two sensing array which point out different temperature measurements due to the difference distance from the ablation point.

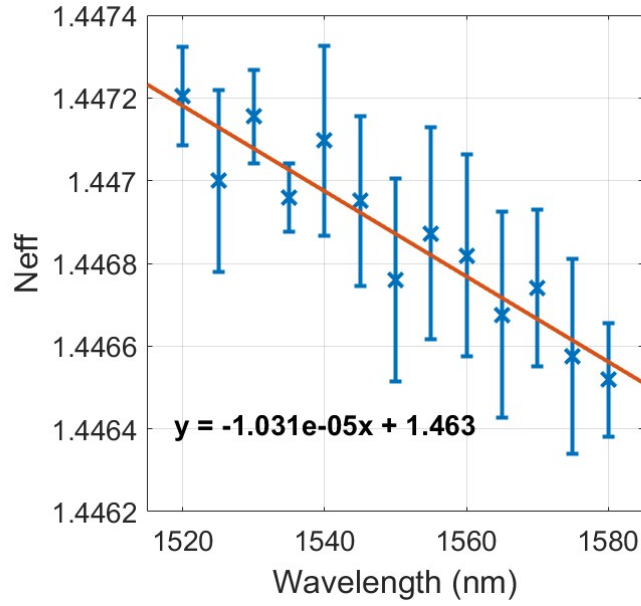


Figure 3.43: First order polynomial interpolation of n_{eff} values for different wavelengths considering all the nine fabricated array.

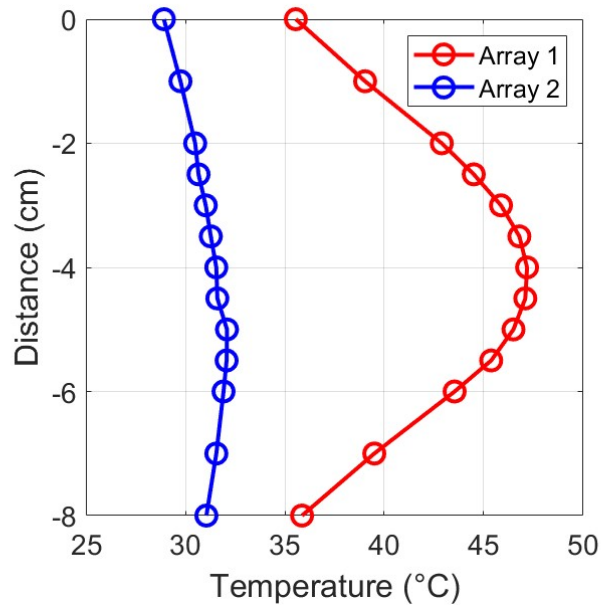


Figure 3.44: Sensing FBG arrays measuring temperature profiles.

3.6.1 Calibration procedure of the temperature sensor

The final sensor has been encapsulated in a 120 mm long glass capillary with diameter equal to 1 mm ensuring both small thermal inertia and a stronger packaging to protect the bare sensing fiber avoiding damages during usage (Fig. 3.45)

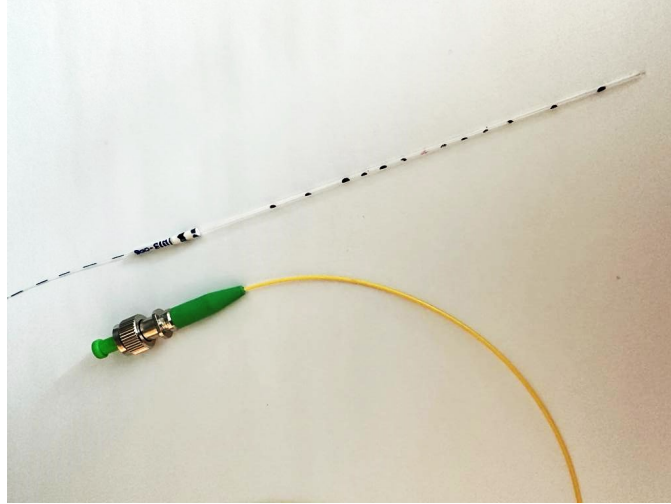


Figure 3.45: Multipoint temperature sensor.

Considering the encapsulated sensor all the 13 gratings have been calibrated as temperature sensors using a *Thorlabs PTC1/M Temperature-Controlled Mini-Series Breadboard* opportunely programmed to generate different steps from 15 °C to 45 °C (Fig. 3.46) while the wavelength shift of the gratings λ_{bragg} is measured using a *Micron Optic Optical Sensing Interrogator sm125*.

As a second step the empirical calibration curve (Fig. 3.47) has been computed using the a first order polynomial interpolating algorithm whose coefficient are reported in the following Tab. 3.3. which are closed to the the theoretical sensitivity of 100 pm/°C.

Further the temperature measured with the optical sensing array has been compared with the measurements obtained using the reference sensor of the thermal board. In details the wavelengths are converted into the temperature values using the previously computed conversion coefficients. (Fig. 3.48)

In conclusion considering up to 72 steps in which the temperature is kept constant the accuracy of the FBGs have been evaluated showing a good result lower than 0.1 °C as reported in Fig. 3.49

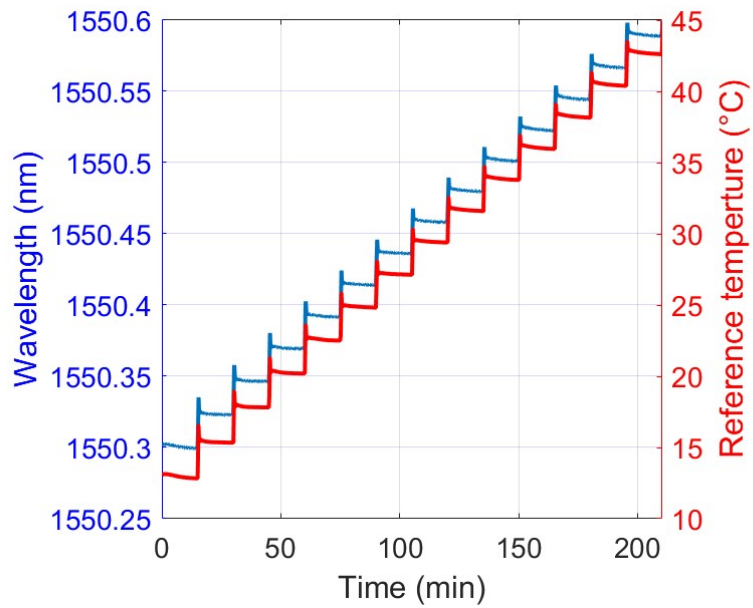


Figure 3.46: Calibration steps: wavelength vs reference temperature.

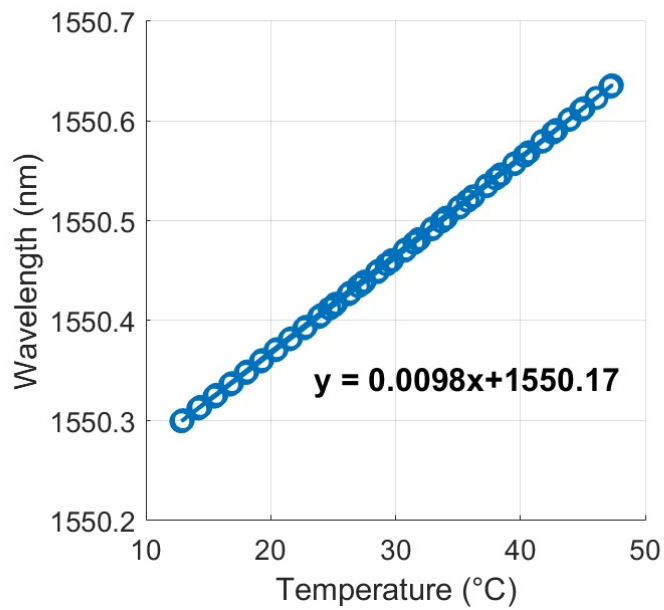


Figure 3.47: Calibration curve of the temperature sensor.

Sensitivity K (nm/°C)	Lambda_0 (nm)
0.00943	1520.43
0.00952	1525.25
0.00953	1530.37
0.00969	1535.15
0.00975	1540.26
0.00972	1545.13
0.00976	1550.17
0.00974	1555.09
0.00973	1560.13
0.00963	1564.88
0.00969	1569.73
0.00978	1574.67
0.00988	1579.61

Table 3.3: Measured temperature sensitivity coefficients.

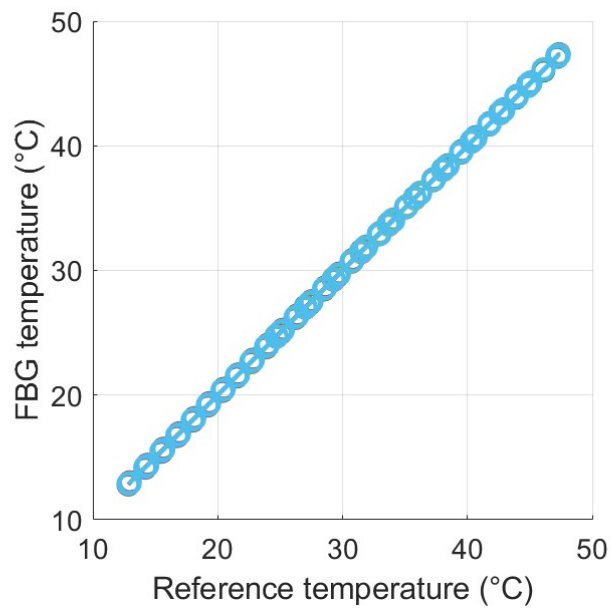


Figure 3.48: Optical sensor versus reference sensor in measuring temperature.

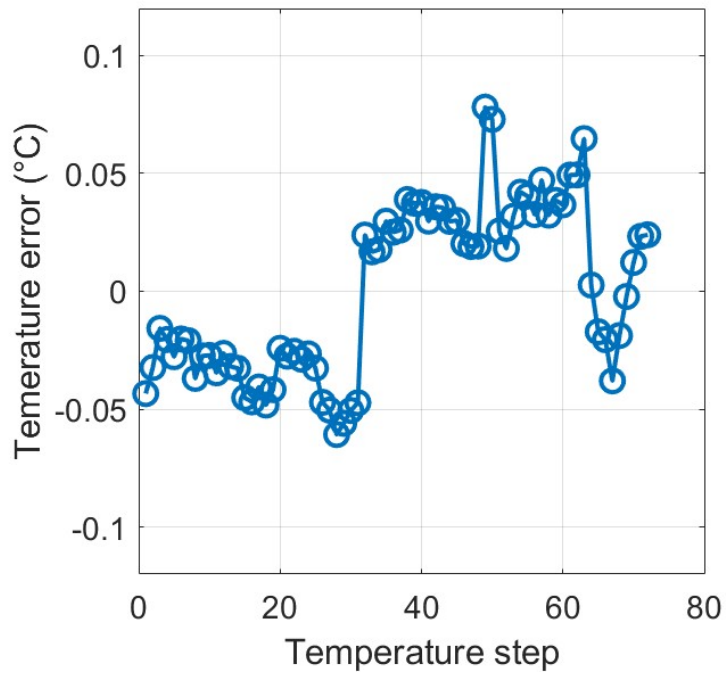


Figure 3.49: Optical temperature sensor accuracy.

Chapter 4

SMS theoretical background

In this section is described the working principles of a inline infermometric sensor made by offset splicing a multimode fiber section between two single mode fibers as shown in Fig. 4.1.



Figure 4.1: Schematic of the SMS structure.

The obtained structure (SMS) works as an interferometer since the modes in the MM section due to their different phase velocity during the propagation acquire a phase shift provoking an interference pattern which results in a change of power value in the field propagating in the next SM section [20]. According to this the MM section represents the sensing unit of the sensor and any perturbation including the effects of temperature and strain can be read as a shift in the interference pattern. In details the first SM-MM junction works as a splitter [20] in fact since the first section is a single mode fiber only the LP01 mode can propagate but at the junction the input power is splitted, according to their overlap integral, between the two modes that are now allowed to propagate. From the other hand the second junction MM-SM works as a combiner since only the LP01 can propagate again in the other single mode section whose length is properly computed to properly attenuate all the higher order modes. To be more precise the offset splice excites an infinite number of modes so the MM fiber has to be chosen carefully with an appropriate cut off wavelength able to guarantee the propagation of only two modes in the desired wavelength range despite the short length.

To analyse this sensor is possible to simplify the multi-mode section as an exactly two mode propagating fiber according to this model the output power is proportional to the following expression:

$$P_{out} \propto P_{in}(1 + \Psi^2 + 2\Psi \cos \phi) \quad (4.1)$$

In details ϕ is the parameter representing the acquired phase difference between the two modes which depends on wavelength and the propagation length while the coefficient Ψ depends on the coupling between the two modes [20]. (Fig. 5.2)

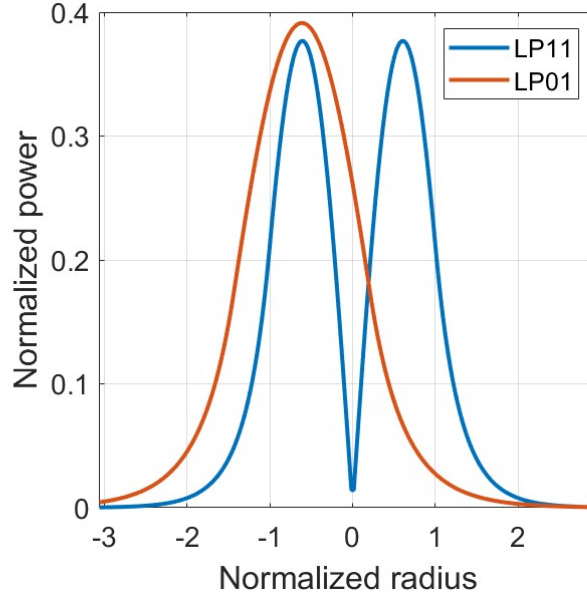


Figure 4.2: Matlab simulation showing modal profiles during the computation of the overlap integral.

Analysing the output spectrum is possible to notice a common pattern characterized by spectral fringes whose free spectral range (FSR) can be approximated with the following expression [20]:

$$FSR \simeq \frac{\lambda^2}{2\Delta L \Delta_{neff,01-11}} \quad (4.2)$$

As a result of this the FSR shows higher values as the considered λ increase up to the cut off wavelength which is the boundary between multimode and single mode behaviour. Furthermore considering a given wavelength range for example 1500 nm-1600 nm which is the measuring range of the *125si Micron optic*. The number of peaks is strictly related to the difference (Δn_{eff}) between the n_{eff} of the two modes that depends on the specific used fiber and the length of the MM section (ΔL) which is an easy way to control the number number of peaks in the output spectrum (Fig. 4.3)

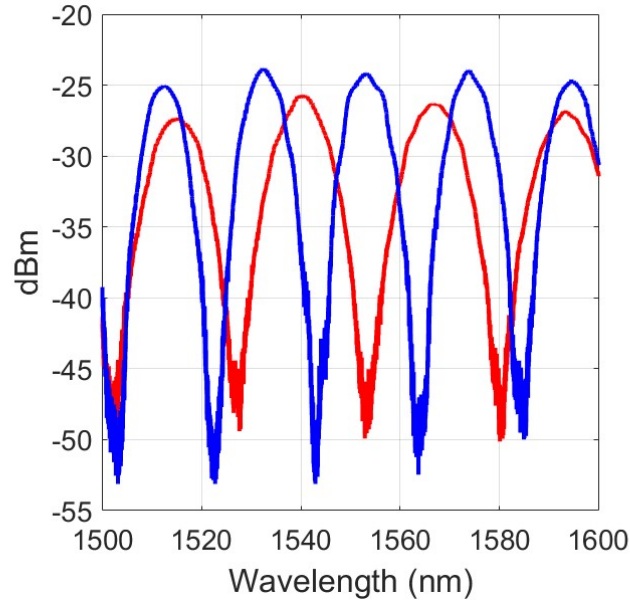


Figure 4.3: Measured spectrum of SMS realized using different multimode section length.

Chapter 5

SMS fabrication

In this section is analysed the fabrication process of the inline interferometric sensor made by offset splicing a multimode fiber section between two single mode fibers. As a preliminary step a *Matlab* model was coded to theoretically simulate the modal field distribution, the overlap integral between the two modes at the offset junction and their propagation in the MM fiber which are useful to correctly design the SMS parameters.

One of the most critical parameters in designing a SMS is the offset value of the junction between the single mode and the multimode section since it determinates the excitation of the LP11 mode. In fact as reported in Fig. 5.1 since there is no offset the overlap integral between the input LP01 mode and the higher mode tends to zero while in Fig. 5.2 where an offset equal to $3\ \mu\text{m}$ is used also the higher mode LP11 is excited.

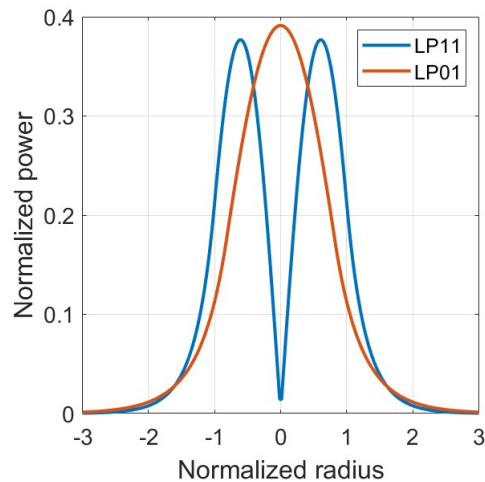


Figure 5.1: Matlab simulation to compute the overlap integral between two modes in a common splice

The basic idea in designing the offset junction for a SMS structure is to overlap the LP01 peak with one of the lobes of the higher order mode maximizing the coupling

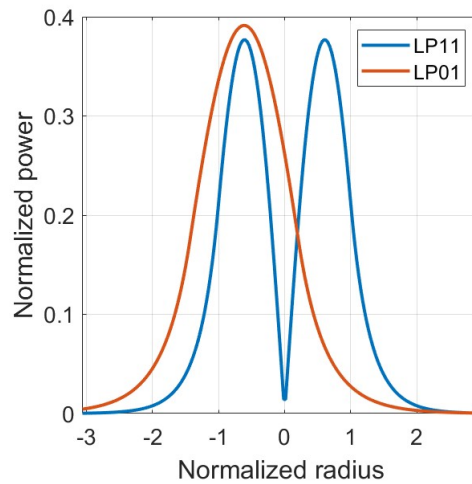


Figure 5.2: Matlab simulation to compute the overlap integral between two modes in a offset splice.

between the two modes. In details the best result are obtained for an *offset* $\simeq 4\ \mu\text{m}$ generating well defined bi-modal interference and a contrast between maxima and minima higher than 10 dB. This junction using standard $250\ \mu\text{m}$ fiber can be done using a common splicer such as the *Fujikura 90s* reducing significantly the fabrication costs respect to the FBGs. In details the splicer works firstly aligning the core profiles of the two fiber and once this step is correctly performed the two sections are shifted by the desired value. The offset junction visualized through the splicer camera is reported in Fig. 5.3 where the two spliced fibers are displayed at the end of their fusing process.

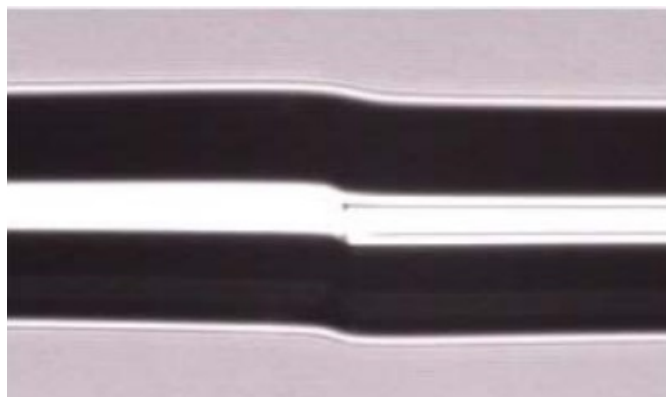


Figure 5.3: Fujikura 90s splicer camera displaying an offset junction.

5.0.1 SMS using SM2000 fiber for the multimode section

In this section is presented a SMS sensing structure in which the SM2000 fiber, described in chapter.3 is used as multimode fiber section between two SFM28 single mode pigtails. Since the goal is the realization a novel cost effectively sensing structure in the range 1500 nm-1600 nm, the cut off wavelength value of the SM2000 fiber perfectly match this constrain ensuring the desired two mode behaviour for wavelength shorter than 1750 nm.

Fig. 5.6 shows this aspect since the interference pattern appears clearly only in the wavelength range where the fiber supports the propagation of only two-modes. In details the V number in that range is confined between $V \simeq 3.5$ beyond which higher order modes such as LP21, LP20 can propagate and $V = 2.4$ which indicates the beginning of the single mode region. However a lot of attention should be paid in designing the length of the MM section since a too short one may not attenuate enough the undesired higher order modes badly compromising the working principle of the sensing structure.

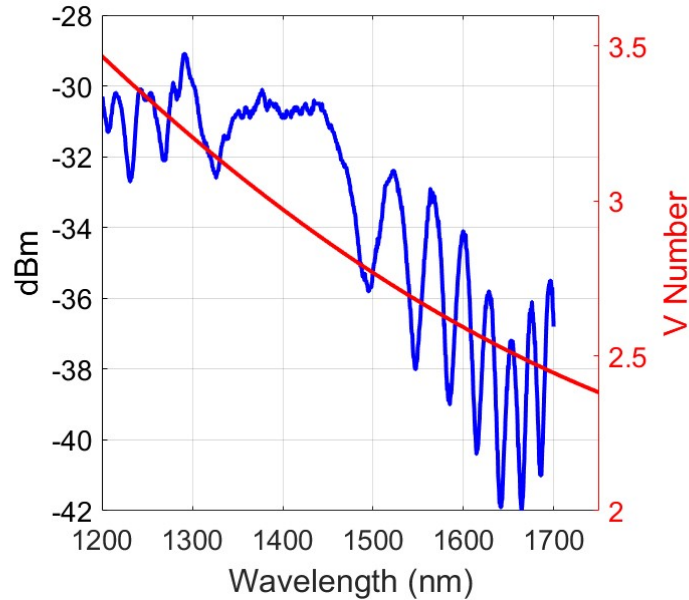


Figure 5.4: SMS interference pattern respect to V number.

The main drawback of using the SM2000 fiber for the MM section in is the too high required MM section length necessary to obtain an interference spectrum where the maxima can be clearly detected with low levels of uncertainty. As an example Fig. 5.5 highlights an interference spectrum which is supposed to work well since its maxima, spaced by a $FSR \simeq 20$ nm can be easily detected clearly measuring any shift due to physical perturbation in the sensing MM section. However to obtain the described spectrum a 17.5 cm long SM2000 section is used making the sensor unmanageable and quiet difficult to embed. This aspect results very limiting since the most important features in using fiber optic sensor respect to most common electro-mechanical solutions is the small size and

the easy integration in different structures including biological tissues.

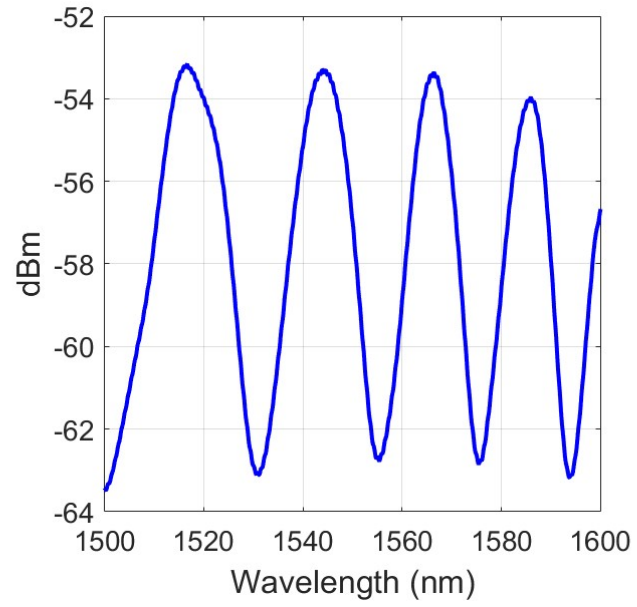


Figure 5.5: Interference spectrum of a SM2000 SMS.

5.0.2 SMS using BIF G657 fiber for the multimode section

To overcome the limits related to the too long required MM section using the SM2000 fiber the possibility of using a bend insensitive fiber is also investigated. Nominally the theoretical cut off value indicated in the data-sheet of the *Prysmian G657* is 1300 nm so in the wavelength range 1500 nm - 1600 nm the fiber works as a single mode guide and as a consequence the SMS is theoretically supposed to be realizable only for shorter wavelength (Fig. 5.6).

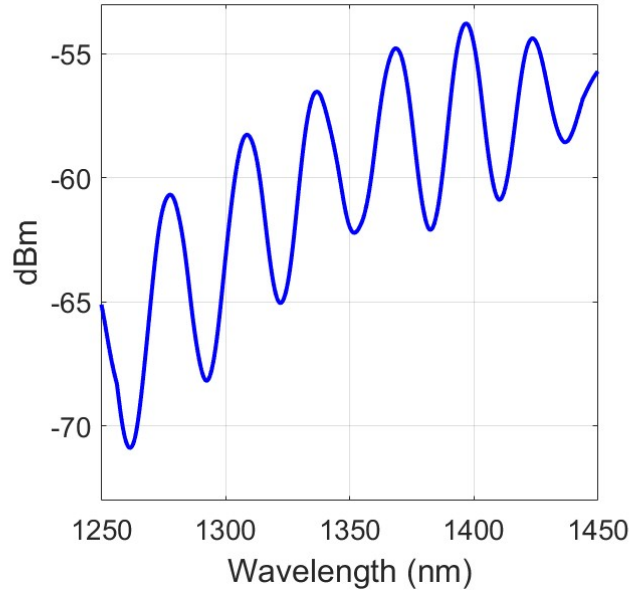


Figure 5.6: SM2000 SMS interference pattern respect to V number.

However given an opportune short length, the bend-insensitive section supports the propagation of two modes, which propagate at two different phase velocities and then interfere obtaining the same pattern. Furthermore the use of this fiber guarantees all the benefits described in chapter3 in reducing the bend losses and disturbances.

Fig. 5.7 compares the output spectra of two 5 cm long MM section SMS sensors using at first the SM2000 (red) which presents a patten with $FSR \simeq 70$ nm suffering the limits previously exposed in detecting the maxima and their shift. Secondly the BIF G657 (blue), where the FSR is now reduced to a value $\simeq 30$ nm and the maxima can be easily detected with low level of uncertainty.

The reduced FSR for the BIF G657 case can be explained considered the Eq. 4.2 in fact since the two modes have an higher Δ_{neff} respect to the SM2000 is possible to obtain a well defined interference spectrum despite the short length encouraging the sensor embedding thanks to its reduced size.

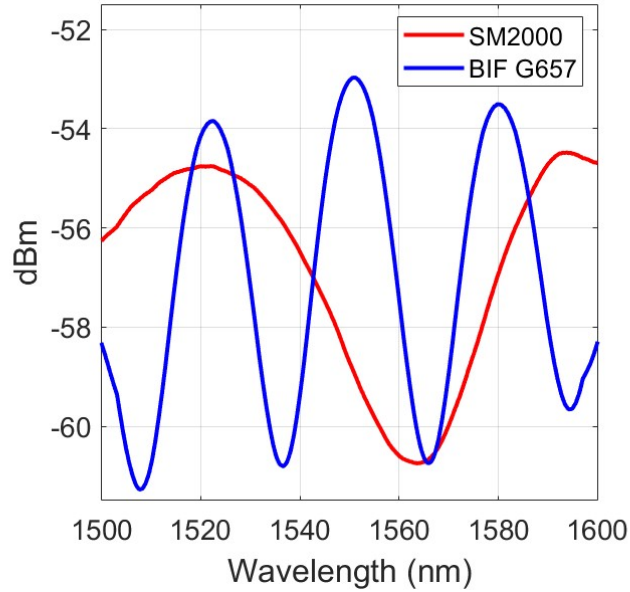


Figure 5.7: Interference pattern of SM2000 SMS respect to BIF G657 case.

5.0.3 BIF G657 SMS temperature sensor

In this section is presented an implementation of the BIF G657 SMS as cost effective temperature sensor. The major benefit in using an interferometric sensor [20] is the higher sensitivity respect to the FBGs, which since are the most widespread fiber optic sensor are considered as a reference. In details the SMS shows a theoretical temperature sensitivity up to $100 \text{ pm}/^\circ\text{C}$; moreover the possibility of fabricate the sensor using only a conventional fusion splicer makes the SMS sensing structure very competitive among the fiber optic sensors.

The SMS has been tested using the *Thorlabs PTC1/M Temperature-Controlled Mini-Series Breadboard* while the shift of the interference spectrum is measured using a *Micron Optic Optical Sensing Interrogator sm125*. Fig. 5.8 and Fig. 5.9 show the measured shift for different temperature values 20°C , 30°C and 40°C .

Later the the SMS sensor is evaluated performing several steps 5°C spaced from 15°C to 45°C . The monitored peak wavelength is than compared to the temperature measured by the reference sensor (Fig. 5.10). The empirical calibration curve is reported in Fig. 5.11 showing as expected a temperature sensitivity equal to $0.84 \text{ pm}/^\circ\text{C}$ which results much more higher than the one measured for the FBGs in Chapter 3.

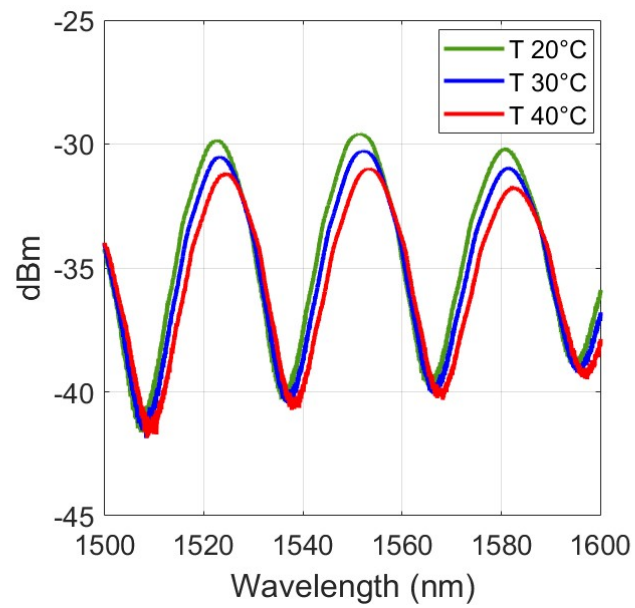


Figure 5.8: Measured spectra of the SMS interference pattern for different temperature values.

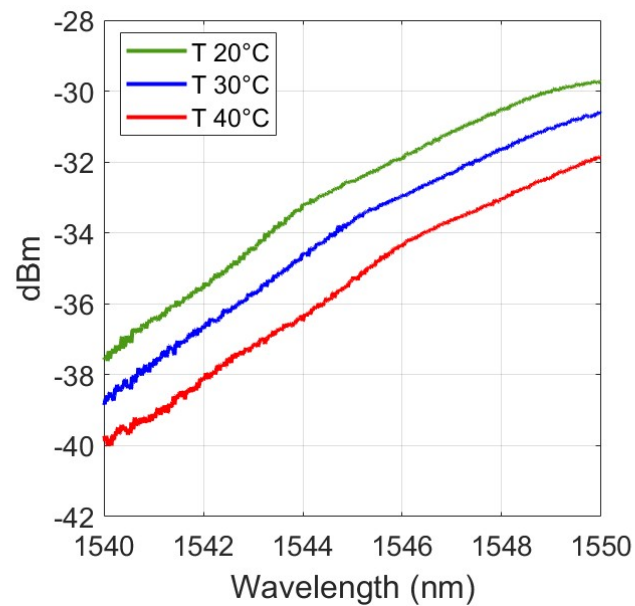


Figure 5.9: Details on the measured spectra of the SMS interference pattern for different temperature values.

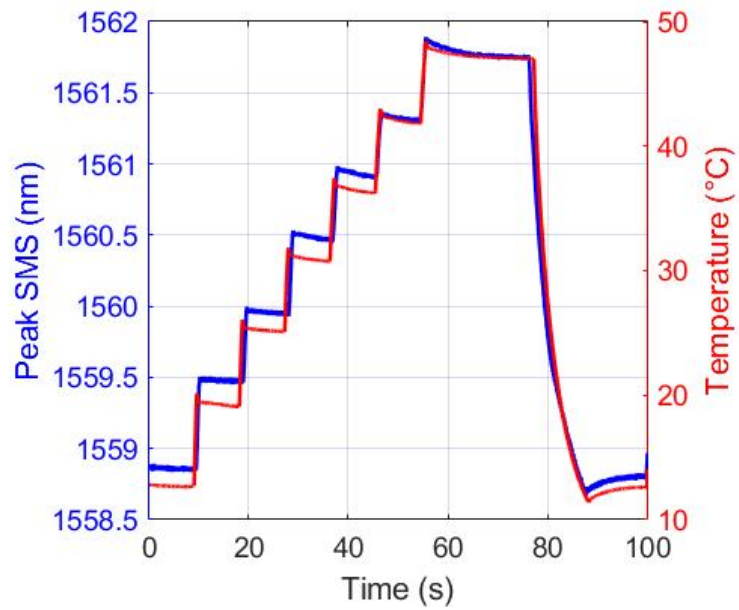


Figure 5.10: SMS peak wavelength measured for different temperature steps.

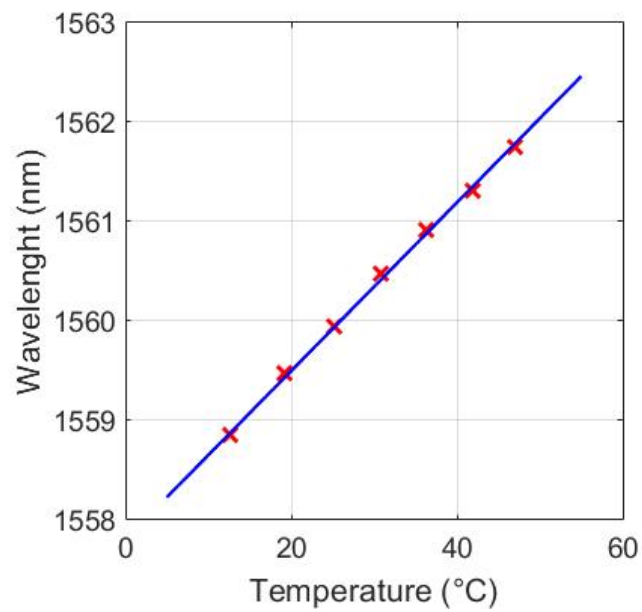


Figure 5.11: Calibration curve of the SMS used as temperature sensor.

Chapter 6

Optical flow-meter

In this chapter is presented the realization of the optical version of the hot wire flow-meter [21] in which the flow of air is measured by the temperature changed caused by flowing air dissipating heat. To fabricate this a 9xx diode laser controlled by a fixed current (around 1 A) is used as heating source while the sensing unit, which is used to measure the temperature induced variations, can be realized using both FBG and the SMS structure presented in chapter. 4.

One of the most challenging constrain is the realization of a single device combining in the same fiber the sensing unit and the heating source. This solution allows the elimination of the air gap responsible of the convective motions between the pump fiber and the sensing unit which provokes a too large thermal transitory (> 20 s) limiting the sensor performances.

6.1 FBG fast response flow-meter

In order fabricate a optical hot wire flow meter with a very fast transitory, is analysed the possibility of using a double cladding fiber combining in the same device the sensing unit in the core and the laser pump acting as heating source in the first cladding. Specifically a high precise 1550 nm FBG was written into the nlight 20/125 DC fiber core. This is a challenging goal since the fiber presenting a normalized frequency $V > 2.4$ ($V \simeq 3.25$) works has a multi-mode guide. This allows the propagation of higher order modes, which propagating with different phase velocities match the Bragg condition for different wavelengths inducing unde- sired back reflections.

In addition to enhance the thermal conversion of the laser source into heat the cladding region surrounding the grating was laser inscribed to induce higher pump losses and secondly all the sensing unit was covered by a graphite film.

The sensor require a quiet expensive setup (Fig. 6.2) due to the need of a combiner which is a optical device used to combine the laser pump and the sensing signal into the double cladding fiber.

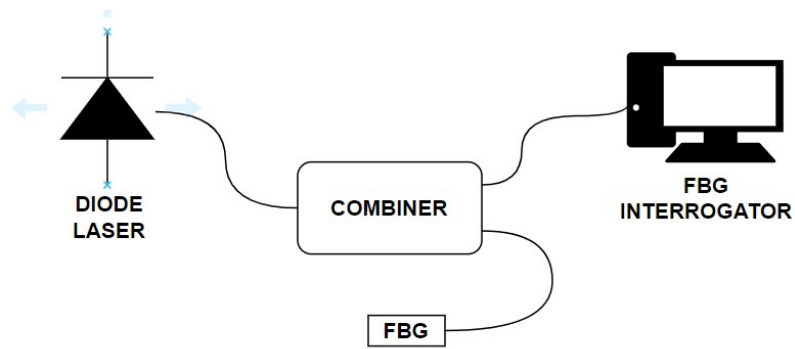


Figure 6.1: Schematic of the FBG hot-wire flow-meter.

The sensing unit which presents a very small size (diameter lower than $250\ \mu\text{m}$ and a length equal to $2\ \text{mm}$) is inserted in a 3D-printed packaging so that the entire sensor can be easily installed in a common pipe

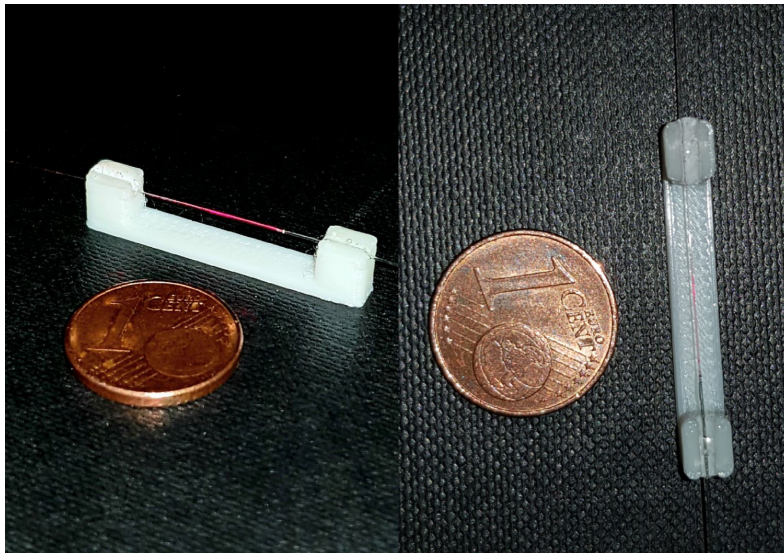


Figure 6.2: Hot wired FBG sensing unit.

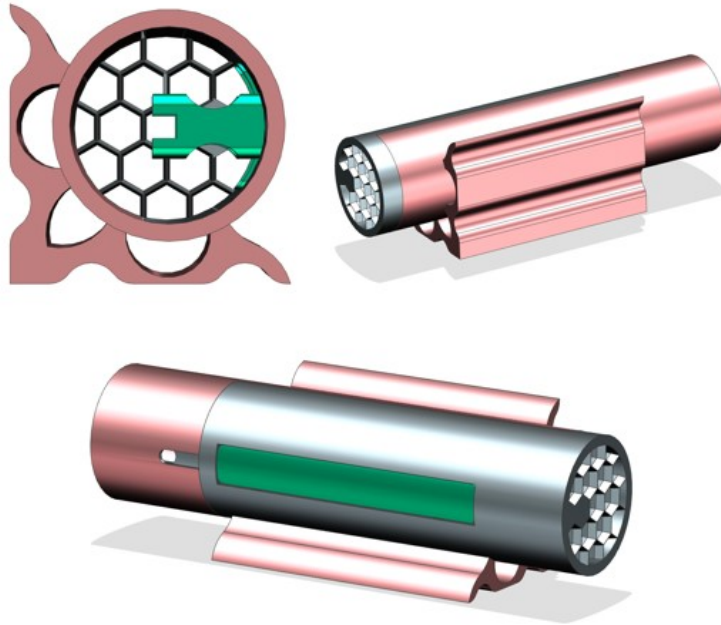


Figure 6.3: Schematic of the FBG hot-wire flow-meter.

The entire sensor including its packaging was added in a pipe and compared to a commercial flow-meter used as a reference sensor. A voltage controlled pump is used as a flow generator to provide different steps with constant flux as pipe input. As reported in Fig. 6.4 the optical version of the sensor show a the measured wavelength shift with a quick response time very closed to the one of the reference sensors which is lower than 300 ms.

Although the measurements show a non-linear behaviour due to the dissipative effects these preliminary results demonstrate the feasibility of the design offering remarkable advantages in applications where remote and electromagnetically immune operations are required. Moreover this single point design taking example from the sensing FBG array configuration describe in chapter. 3 can be in future researches improved developing a multi-point design able to efficiently monitor the profile of flux flowing in pipes.

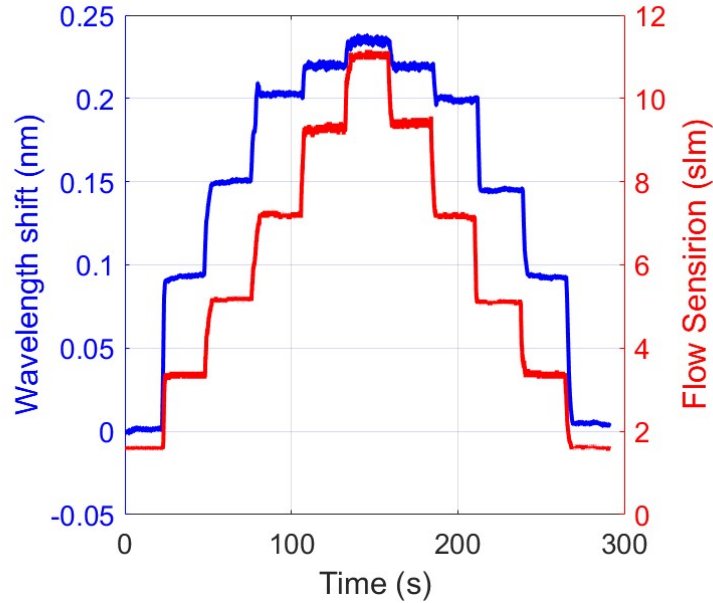


Figure 6.4: Optical flow-meter versus reference sensor.

6.2 SMS parallel fibers flow meter

In this section is investigated the possibility of realizing a cost effective optical flow-meter eliminating the combiner used in the other configuration which is an expensive component limiting its applicability.

In this solution called parallel fibers, the diode laser delivering fiber is opportunely inscribed with the femtosecond laser in 10 cm long section to increase the thermal conversion of the laser pump into heat. Secondly a 10 cm long BIF G657 SMS is realized and the two fiber are encapsulated in the same capillary limiting as much as possible the air gap. However as reported in Fig. 6.5, where the sensor is tested in the same way as done in the previous section, exhibits a response time lower than 20s which is a too long time limiting the applicability of the sensor especially as respiratory device since a much faster transitory is needed.

In details looking at Fig. 6.5 the parameter called "Difference Peak SMS" is computed making the difference between the peak of a SMS used to monitor the room temperature defined as "cold_point" and the SMS inserted in the capillary referred as "hot_point". According to this due to the heating pump the hot_point SMS is subjected to a greater red wavelength shift. In conclusion when the flowing flux tends to zero the peak difference between the two sensors is maximized as correctly reported in the graph. In the right vertical axis of Fig. 6.5 is reported the reference flow whose measurements are expressed using negative values since the used commercial sensor is a directional device distinguishing if the flux is flowing from port 1 to 2 or vice-versa.

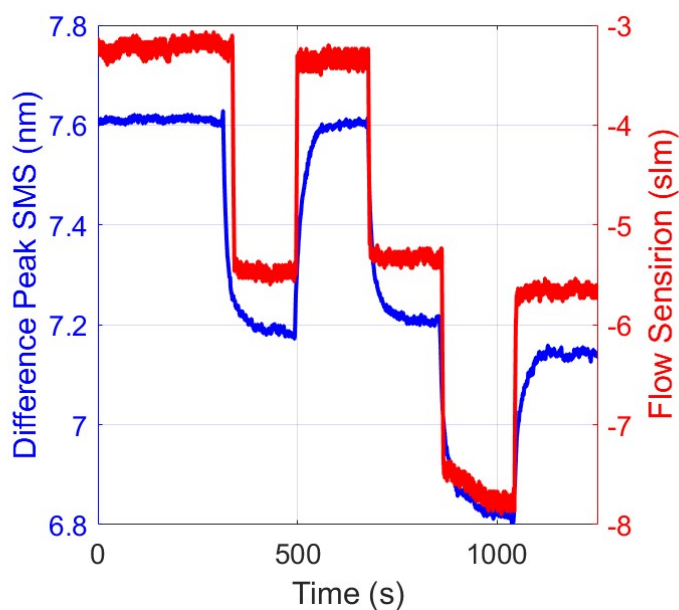


Figure 6.5: SMS optical flowmeter versus reference sensor.

Chapter 7

Conclusion

The acquire know how has encouraged the FBGs realization in different fiber types including polyamide coated, bend insensitive, multimode and also double cladding fibers fitting in a better way the required constrains of novel sensors

7.1 Achieved results

The most important result consists in the development and optimization of the femtosecond laser fabrication technique which allows to produce high precise application specific FBGs whose quality in terms of reflectivity closed to 90-95%, side lobes attenuation > 15 dB, FWHM < 400 pm can be straightly compered with common grating available in the optical components market

For what concerns the applicability the realization of the 13 points FBG sensing array highlight encouraging results in terms of accuracy less than 0.1 °C, linearity and repeatability. Moreover it shows the goodness of the sensor design in monitoring temperature profiles and distributed measurements.

The investigated novel inline SMS interferometer suggests the feasibility in fabricating economic optic sensors alternative to the most common FBG, showing also a temperature sensitivity 10 times higher than the FBGs. However the required multimode section length ($\simeq 10$ cm) represents the main drawback limiting its handling

7.2 Outlook

This thesis opens to future analysis in particular the femtosecond laser fabrication technique can be further developed increasing the gratings quality reaching higher standard in the optical components market. Moreover the availability of higher quality FBGs allows the development of more and more accurate sensor in several application fields

The flowmeter prototype represents the feasibility of the optical version of the hot wire flow-meter highlighting the applicability of FBGs into different fields respect to the more common temperature and strain monitoring. However it requires deeper calibration analyses in order to include in its future releases temperature compensation, ability in disambiguate the flux propagating direction and a multipoint sensing design.

In addition the availability or the development of high accuracy low cost interrogation setup represents the critical turning point for the FOS. In fact as main drawback FBGs like many other optical devices required costly interrogation devices drastically disadvantaging the optical version of the sensors respect to their electrical counterparts.

In conclusion optical fiber sensors have successfully entered several critical application fields and markets because they can overcome limitations of their conventional counterparts with an electrical readout. In particular, harsh environments as well as biomedical applications, thanks to remote interrogation, electromagnetic interference-proof functionality and no direct electrical power supply, may greatly benefit from the replacement of an electric readout sensor with an optical fibre-based version.

Bibliography

- [1] Z. Ma and X. Chen, “Analysis of distributed measurement method for array antenna position,” 2020.
- [2] S. J. Mihailov, “Fiber bragg grating sensors for harsh environments,” *Sensors*, vol. 12, no. 2, pp. 1898–1918, 2012.
- [3] H.-E. Joe, H. Yun, S.-H. Jo, M. B. Jun, and B.-K. Min, “A review on optical fiber sensors for environmental monitoring,” *International journal of precision engineering and manufacturing-green technology*, vol. 5, pp. 173–191, 2018.
- [4] K. O. Hill and G. Meltz, “Fiber bragg grating technology fundamentals and overview,” *Journal of lightwave technology*, vol. 15, no. 8, pp. 1263–1276, 1997.
- [5] J. Chen, B. Liu, and H. Zhang, “Review of fiber bragg grating sensor technology,” *Frontiers of Optoelectronics in China*, vol. 4, pp. 204–212, 2011.
- [6] R. Kashyap, “Chapter 2 - photosensitivity and photosensitization of optical fibers,” pp. 15–51, 2010.
- [7] A. Othonos, “Fiber bragg gratings,” *Review of scientific instruments*, vol. 68, no. 12, pp. 4309–4341, 1997.
- [8] R. Kashyap and J. Lopez-Higuera, “Fiber grating technology: Theory, photosensitivity, fabrication and characterization,” *Handbook of Optical Fibre Sensing Technology*, pp. 349–374, 2002.
- [9] T. Erdogan, “Fiber grating spectra,” *Journal of lightwave technology*, vol. 15, no. 8, pp. 1277–1294, 1997.
- [10] K. O. Hill, Y. Fujii, D. C. Johnson, and B. S. Kawasaki, “Photosensitivity in optical fiber waveguides: Application to reflection filter fabrication,” *Applied physics letters*, vol. 32, no. 10, pp. 647–649, 1978.
- [11] D. Lam and B. K. Garside, “Characterization of single-mode optical fiber filters,” *Applied optics*, vol. 20, no. 3, pp. 440–445, 1981.
- [12] V. Murukeshan, P. Chan, L. S. Ong, and A. Asundi, “Intracore fiber bragg gratings for strain measurement in embedded composite structures,” *Applied optics*, vol. 40, no. 1, pp. 145–149, 2001.
- [13] S. Pal, T. Sun, K. T. Grattan, S. A. Wade, S. F. Collins, G. W. Baxter, B. Dussardier, and G. Monnom, “Strain-independent temperature measurement using a type-i and type-ii optical fiber bragg grating combination,” *Review of Scientific Instruments*, vol. 75, no. 5, pp. 1327–1331, 2004.
- [14] A. Bertholds and R. Dandliker, “Determination of the individual strain-optic coefficients in single-mode optical fibres,” *Journal of lightwave technology*, vol. 6, no. 1, pp. 17–20, 1988.

- [15] D. Anderson, V. Mizrahi, T. Erdogan, and A. White, "Production of in-fibre gratings using a diffractive optical element," *Electronics Letters*, vol. 6, no. 29, pp. 566–568, 1993.
- [16] J. Albert, S. Theriault, F. Bilodeau, D. Johnson, K. Hill, P. Sixt, and M. Rooks, "Minimization of phase errors in long fiber bragg grating phase masks made using electron beam lithography," *IEEE Photonics Technology Letters*, vol. 8, no. 10, pp. 1334–1336, 1996.
- [17] K. P. Chen, P. R. Herman, and R. Tam, "Strong fiber bragg grating fabrication by hybrid 157-and 248-nm laser exposure," *IEEE Photonics Technology Letters*, vol. 14, no. 2, pp. 170–172, 2002.
- [18] B. Malo, K. O. Hill, F. Bilodeau, D. Johnson, and J. Albert, "Point-by-point fabrication of micro-bragg gratings in photosensitive fibre using single excimer pulse refractive index modification techniques," *Electronics Letters*, vol. 18, no. 29, pp. 1668–1669, 1993.
- [19] A. Martinez, I. Khrushchev, and I. Bennion, "Thermal properties of fibre bragg gratings inscribed point-by-point by infrared femtosecond laser," *Electronics letters*, vol. 41, no. 4, pp. 176–178, 2005.
- [20] M. Olivero, A. Vallan, R. Orta, and G. Perrone, "Single-mode-multimode-single-mode optical fiber sensing structure with quasi-two-mode fibers," *IEEE Transactions on Instrumentation and Measurement*, vol. 67, no. 5, pp. 1223–1229, 2018.
- [21] X. Jiang, K. Wang, J. Li, H. Zhan, Z. Song, G. Che, and G. Lyu, "Optical sensor of thermal gas flow based on fiber bragg grating," *Sensors*, vol. 17, no. 2, p. 374, 2017.